Contract No.:

This manuscript has been authored by Battelle Savannah River Alliance (BSRA), LLC under Contract No. 89303321CEM000080 with the U.S. Department of Energy (DOE) Office of Environmental Management (EM).

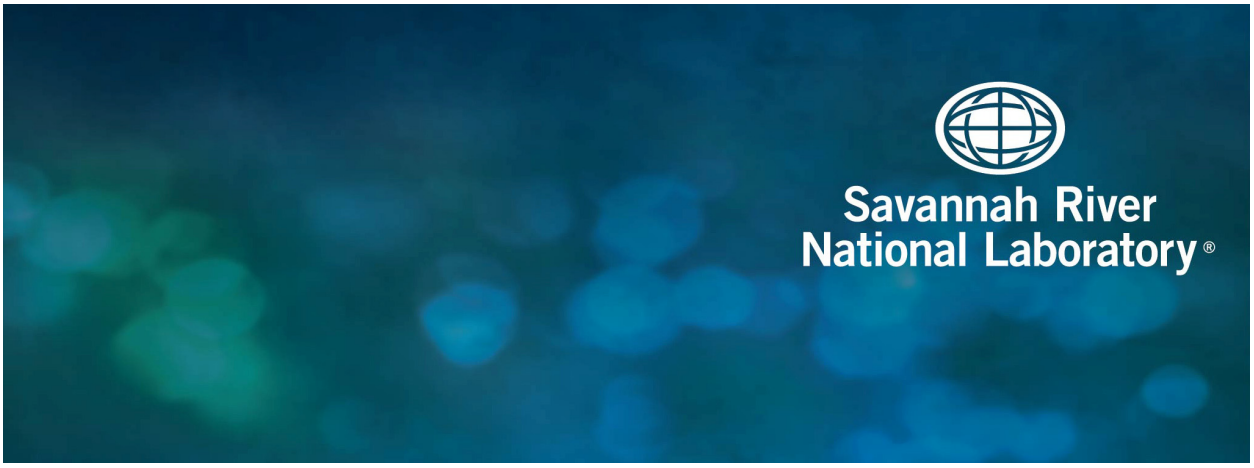

A U.S. DEPARTMENT OF ENERGY NATIONAL LAB • SAVANNAH RIVER SITE • AIKEN, SC • USA

Calibration of Cohesive Parameters for Fracture Test Simulations of Sub-Sized Bend Specimens of AM Steels

Submitted to the
International Journal of Fracture

Shengjia Wu (UM)
Jwo Pan (UM)
Paul Korinko (SRNL)

March 2022
SRNL-STI-2022-00153, Revision 0

This work was produced by Battelle Savannah River Alliance, LLC under Contract No. 89303321CEM000080 with the U.S. Department of Energy. Publisher acknowledges the U.S. Government license to provide public access under the DOE Public Access Plan (http://energy.gov/downloads/doe-public-access-plan).

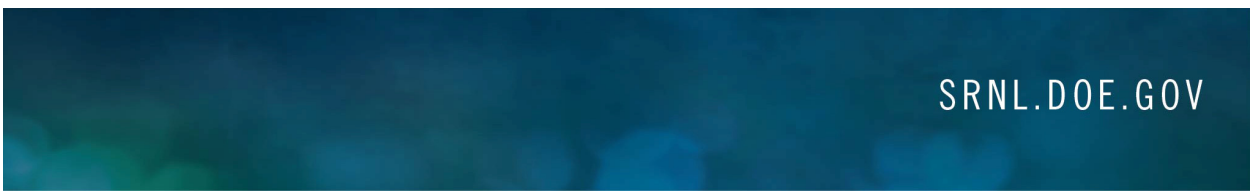

Calibration of Cohesive Parameters for Fracture Test Simulations of Sub-Sized Bend Specimens of AM Steels

Shengjia Wu and Jwo Pan[1]
Mechanical Engineering
University of Michigan
Ann Arbor, MI 48109, USA

Paul S. Korinko
Materials Science and Technology
Savannah River National Laboratory
Aiken, SC 29808, USA

March 17, 2022

Abstract

Crack extensions in sub-sized side-grooved bend specimens of AM steels are examined with changing cohesive parameters. Two-dimensional FE analyses are first conducted to simulate crack extensions by nodal release. The simulation results indicate the near-tip maximum opening stress and separation work rate increase and then slightly decrease for the bend specimens. The hydrogen-charged bend specimens have lower near-tip maximum opening stresses and average separation work rates than those of the uncharged bend specimens. The changing near-tip maximum opening stresses and the separation work rates with increasing crack extension are determined as references for the changing cohesive strengths and energies, respectively. Two-dimensional FE analyses with different changing cohesive parameters are then performed. The simulation results with calibrated cohesive parameters can match well with the test results. The hydrogen-charged specimens have the lower changing cohesive strength vs crack growth curves compared with those of the uncharged specimens. The hydrogen-charged specimens have either lower or similar changing cohesive energy vs crack growth curves

[1] Corresponding author. Tel.:+1-734-764-9404; fax:+1-734-647-3170
Email address: jwo@umich.edu (Jwo Pan)

compared with those of the uncharged specimens. Finally, a three-dimensional FE analysis is conducted to simulate crack extension by nodal release in one bend specimen to examine the stress triaxialities in front of the growing crack fronts at different locations from the center plane to the planes near the side groove front with increasing crack extension to identify possible physical reasons for the changing cohesive parameters.

Keywords: additive manufacturing; changing cohesive parameters; cohesive zone modeling; single edge bend specimen; traction-separation law

1. Introduction

Crack growth in various types of fracture specimens were simulated by the cohesive zone modeling (CZM) approach by many investigators using different traction-separation laws (TSLs). Accurate computational results with the CZM approach for practical applications rely on the two most important cohesive parameters, cohesive energy and cohesive strength, which should be carefully calibrated. Usually, constant cohesive parameters such as constant cohesive strength and cohesive energy were adopted to simulate crack extensions in ductile metals (Roychowdhury et al. 2002; Cornec et al. 2003; Scheider and Brocks 2003, 2006; Sung et al. 2019; Wu et al. 2020). For a fracture specimen or structure, where the size requirements of the plane strain conditions of the linear elastic fracture mechanics are satisfied at crack initiation and during crack extension, the selection of the cohesive energy can be a constant value related to the fracture toughness at crack initiation and during crack extension.

For the failure of ductile metals controlled by the micromechanisms of void growth and coalescence, the Gurson-Tvergaard-Needleman (GTN) model (Gurson 1977; Needleman and

Tvergaard 1987) has been extensively used to model the failure of ductile metals. In GTN model, the mechanical response of a material element is strongly influenced by the stress triaxiality. Therefore, for crack growth in ductile metals using the CZM approach, the cohesive strength and the cohesive energy should also be considered to be stress triaxiality dependent as presented in Siegmund and Brocks (1999, 2000a, 2000b), Anvari et al. (2006), Banerjee and Manivasagam (2009), and Rashid and Banerjee (2017). It should be noted that for the triaxiality-dependent CZM for crack growth simulations in 2-D FE analyses used in Siegmund and Brocks (2000a, 2000b), Anvari et al. (2006), and Rashid and Banerjee (2017), the values of the stress triaxiality at the integration points of the neighboring continuum elements are transported into the corresponding cohesive elements such that the cohesive parameters vary based on different stress triaxialities of the neighboring continuum elements. Recently, Zhang et al. (2020) performed 3-D FE analyses to study the stress triaxiality dependent critical fracture energy and material strength along the tunneled crack front. The computational results in Zhang et al. (2020) suggested that the local fracture energy is a monotonic decreasing function of the stress triaxiality, while the local tensile strength increases linearly with the stress triaxiality.

For the crack growth in a large thin cracked structure, Schwalbe et al. (2013) indicated the 2-D CZM approach for modeling of crack extension should be divided into two regions with different sets of cohesive parameters for the initial flat fracture mode and the subsequent slant fracture mode. Therefore, the cohesive parameters should change from those for flat fracture mode to those for the slant fracture mode for the 2-D CZM approach. Computational results of the crack growth in a large thin cracked structure using changing cohesive parameters for the 2-D plane stress CZM approach can be found in Woelke et al. (2015) and Anderson et al. (2019). For the crack growth in a sub-sized fracture specimen, the majority of the crack front may not be

subjected to the plane strain conditions at crack initiation and during crack extension. As a crack grows in a sub-sized fracture specimen, the stress triaxiality along the crack front changes. Therefore, the cohesive strength and cohesive energy should vary to reflect the change of the constraint conditions along the crack front during crack extension as indicated in Wu et al. (2021).

For a fracture specimen, the plane strain conditions are assumed to prevail along the crack front at crack initiation and during crack extension when the specimen thickness B and the remaining ligament length b are large enough to satisfy

$$B, b > 25\left(J_{0.2}/\sigma_0\right) \tag{1}$$

where σ_0 is the yield stress and $J_{0.2}$ is the intercept of the regression curve of the $J-\Delta a$ data points with the 0.2 mm offset line based on the ASTM Standard E1820 (2020). For a fracture specimen with the sizes not satisfying Equation (1), side-grooves can be introduced to promote a uniform crack front during crack extension but the plane strain conditions along the crack front may not be satisfied.

Wu et al. (2021) simulated crack extensions in sub-sized arc-shaped tension (A(T)) specimens, as discussed in Kim et al. (2004), with the constant and changing cohesive parameters. In contrast to the stress-state dependency of TSL based on the stress triaxiality of the neighboring continuum elements to the cohesive elements used in Siegmund and Brocks (2000a, 2000b), Anvari et al. (2006), and Rashid and Banerjee (2017), Wu et al. (2021) identified the changing cohesive strengths and energies with increasing crack extension based on the changing near-tip maximum opening stresses and separation work rates with increasing crack extension determined by 2-D FE analyses with nodal release as presented in Sung et al. (2021a). The computational load-displacement, load-crack extension, crack extension-displacement and J-

R curves of the A(T) specimens with the selected changing cohesive parameters can fit very well the test data as presented in Wu et al. (2021).

Sung et al. (2019) simulated crack extensions in sub-sized bend specimens with side-grooves made from an additively manufactured (AM) steel plate with the constant cohesive parameters. It should be mentioned that the required specimen sizes of bend specimens based on Equation (1) in Sung et al. (2019) are over 50 mm for the specimens. However, the net thicknesses B_n of these specimens are from 4.630 mm to 4.729 mm. Therefore, the computational load-displacement, load-crack extension, crack extension-displacement and J-R curves of the bend specimens with the selected constant cohesive parameters can only match the general trend of the test data as presented in Sung et al. (2019).

In this investigation, the crack extensions in sub-sized bend specimens made from an AM steel plate are simulated with the changing cohesive parameters to improve the simulation results with the constant cohesive parameters presented in Sung et al. (2019). The experimental set-up and the test results for the sub-sized bend specimens are first briefly presented in Section 2. Then, 2-D FE analyses of the sub-sized bend specimens in different orientations are conducted to simulate crack extensions by nodal release to obtain the changing near-tip maximum opening stresses and separation work rates to account for the changing stress triaxiality with increasing crack extension as presented in Appendix A. The 2-D FE models with a user-defined cohesive element subroutine and the CZM approach with the smooth trapezoidal TSL are presented in Section 3. Next, 2-D FE analyses of the sub-sized bend specimens in different orientations are performed to calibrate changing cohesive strengths and energies in Section 4. In the CZM approach, the stress-state dependency and the 3-D thickness effects enter into the TSL through the changing cohesive strength and cohesive energy based on the trends of the near-tip maximum

opening stress and separation work rate obtained from the nodal release method. In addition, a 3-D FE analysis is conducted to simulate crack extension in one sub-sized bend specimen by nodal release in Section 5. The opening stresses, the out-of-plane stresses and the stress triaxialities in front of the growing crack fronts at different locations from the center plane to the planes near the side groove front with increasing crack extension are examined to identify possible physical reasons for the changing cohesive parameters. Finally, some conclusions are made in Section 6.

2. Experimental Fracture Tests

Fracture tests were conducted using uncharged and hydrogen-charged bend specimens of AM 304 stainless steels as discussed in Sung et al. (2019). The bend specimens were cut in different orientations with respect to the building direction from a fully dense rectangular plate built by LENS (Laser Engineered Net Shaping) which is a type of the directed energy deposition (DED) technology. Fracture tests were first conducted on uncharged bend specimens. Hydrogen-charged bend specimens were then made by charging the specimens with hydrogen to the hydrogen concentration of 2,700 appm for consideration of using the AM steels for hydrogen storage. Figure 1(a) shows a schematic of an AM plate, the definitions of the orientations of the AM plate, and bend specimens made in different orientations. In Figure 1(a), L represents the building direction, S represents the laser scanning or the thickness direction and T represents the width direction. The interfaces between printed layers are schematically represented by gray lines. The orientations of interest are the LS and TS orientations for the bend specimens in this investigation. The schematic plots of two bend specimens in the LS and TS orientations are

shown in Figures 1(b) and 1(c), respectively. The tensile specimens for obtaining the corresponding stress-strain curves are also schematically plotted in Figures 1(b) and 1(c).

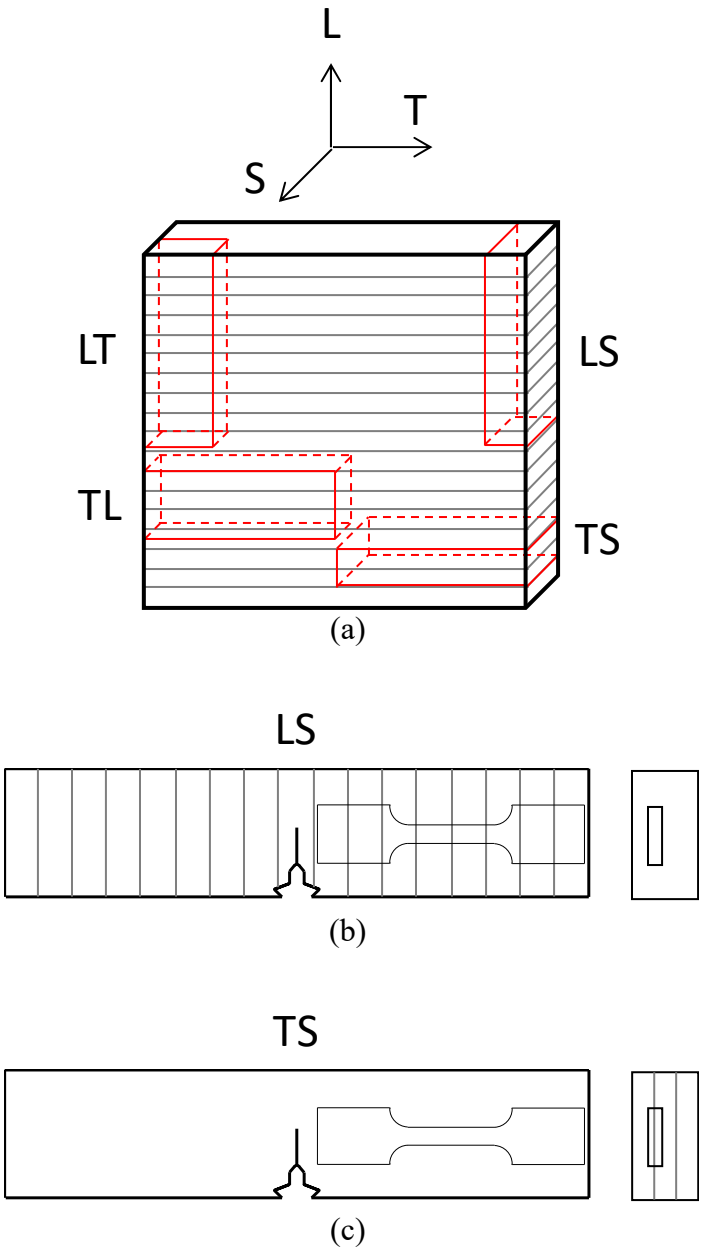

Figure 1. Schematic plots of (a) an AM plate and bend specimens in the (b) LS orientation and (c) TS orientation.

Figure 2 shows a schematic of a bend specimen. One loading pin and two supporting pins are also shown in Figure 2. The bend specimens were made with side-grooves with slightly

different depths. The specimen length L of 49.734 mm and the span S of 43.18 mm between the two supporting pins for all specimens are marked in Figure 2. Table 1 lists the dimensions of the initial crack length a_0, the thickness B, the net thickness B_n, the width W, and the remaining ligament length b for the uncharged and hydrogen-charged bend specimens in the LS and TS orientations. The crack mouth opening displacement (CMOD) was measured by the clip gauge attached to the two notch tips on the lower surface of the bend specimen as shown in Figure 2. The initial CMOD is 2.54 mm.

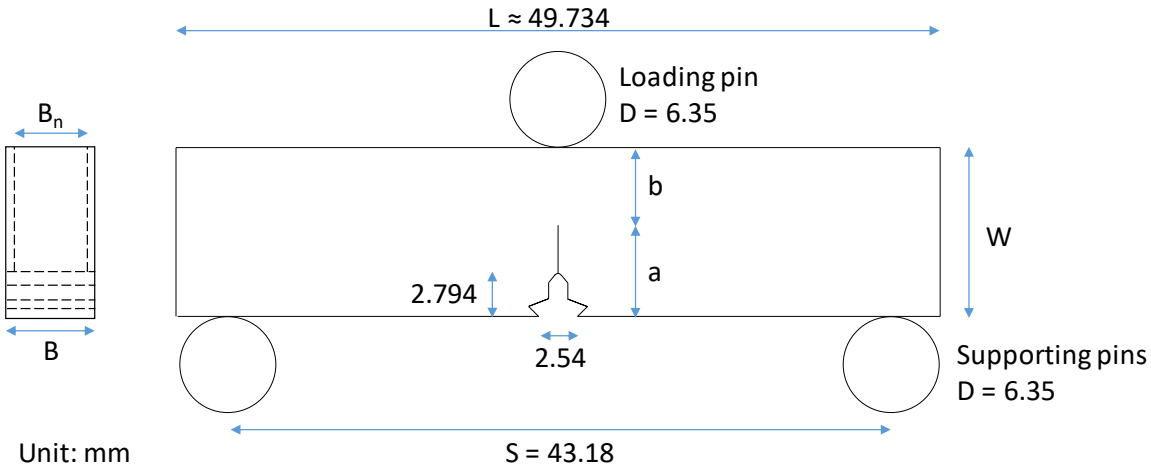

Figure 2. A side-grooved bend specimen.

Table 1. The dimensions for the uncharged and hydrogen-charged LS and TS SE(B) specimens

	LS		TS	
	LS-2 (uncharged)	LS-4 (hydrogen-charged)	TS-2 (uncharged)	TS-4 (hydrogen-charged)
a_0 (mm)	5.939	4.773	5.611	5.669
B (mm)	5.6	5.497	5.532	5.552
B_n (mm)	4.648	4.729	4.63	4.63
W (mm)	10.998	11.148	11.267	11.306
b (mm)	5.059	6.375	5.656	5.637

Figures 3(a) and 3(b) show the experimental set-up for fracture tests of bend specimens. Figure 3(a) shows the crosshead, a loading pin, two supporting pins, and a bend specimen. Figure 3(b) shows the placement of the current wires, voltage wires, and clip gauge for fracture tests. The load measured from the load cell attached to the crosshead, the CMOD obtained by the clip gauge, and the crack extension monitored by an alternating direct current potential drop system based on the ASTM Standard E647 (2015) were recorded during the fracture tests. The test results were presented in Sung et al. (2019). The experimental J-R curves for bend specimens were obtained based on the ASTM Standard E1820 (2020) and presented in Sung et al. (2019). It should be mentioned that changing cohesive parameters will be calibrated to fit the test results for the bend specimens presented in Sung et al. (2019) in this investigation.

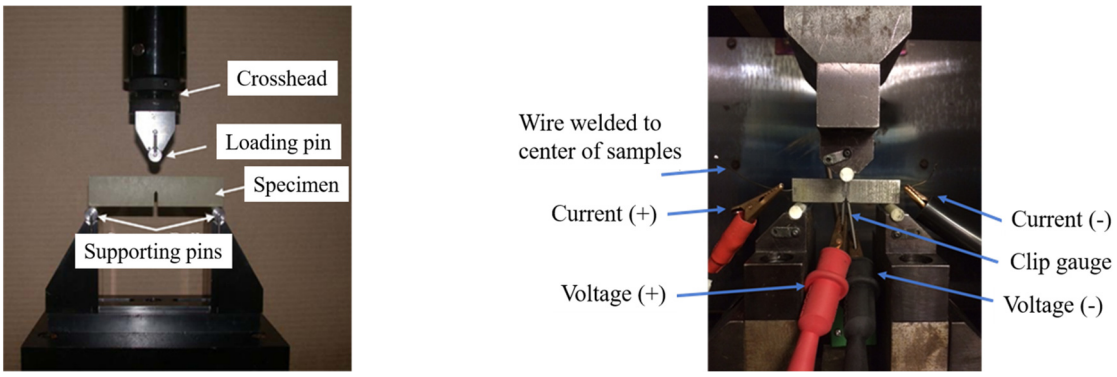

Figure 3. The experimental set-up for fracture tests of bend specimens. (a) Mechanical components of the crosshead, the loading pin, the specimen, and the supporting pins and (b) the placement of the current wires, voltage wires, and clip gauge.

Figures 4(a) and 4(b) show the fracture surfaces of the LS-2 specimen (without charged hydrogen) and LS-4 specimen (with charged hydrogen), respectively. The LS-2 and LS-4 specimens were fatigue pre-cracked to the initial crack fronts as marked in Figures 4(a) and 4(b), respectively. Here, the middle portions of the LS specimens exhibit some necking during the crack extensions and the thicknesses of the specimens near the back surfaces of the specimens close to the loading pin become large due to compression under fully yielded condition (Sung et

al. 2019). The final crack fronts marked in Figure 4 by the heat tinting for the specimens show some reverse tunneling. Figures 5(a) and 5(b) show the fracture surfaces of the TS-2 specimen (without charged hydrogen) and TS-4 specimen (with charged hydrogen), respectively. The TS-2 and TS-4 specimens were also fatigue pre-cracked to the initial crack fronts as marked in Figures 5(a) and 5(b), respectively. Similarly, the middle portions of the TS specimens also exhibit some necking during the crack extensions and the thicknesses of the specimens near the back surfaces of the specimens close to the loading pin also become large due to compression under fully yielded condition (Sung et al. 2019). The final crack fronts marked in Figure 5 by the heat tinting for the specimens also show some reverse tunneling.

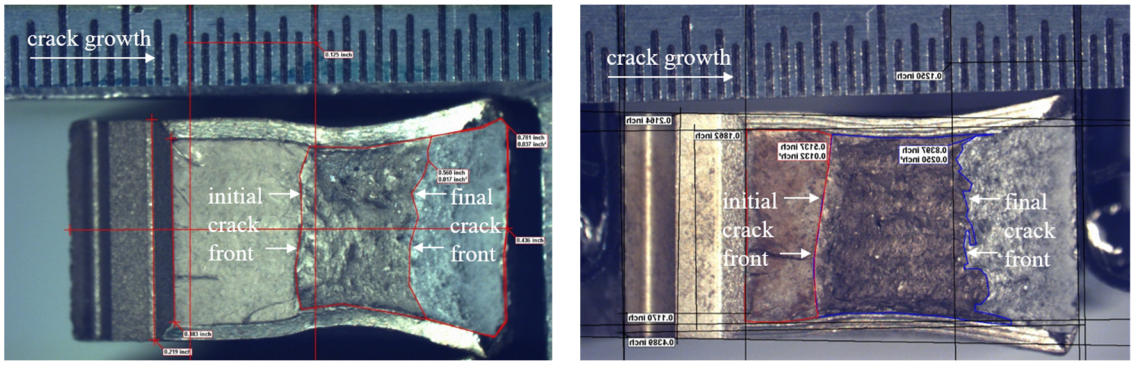

(a) (b)

Figure 4. The fracture surfaces of the (a) LS-2 specimen and (b) LS-4 specimen.

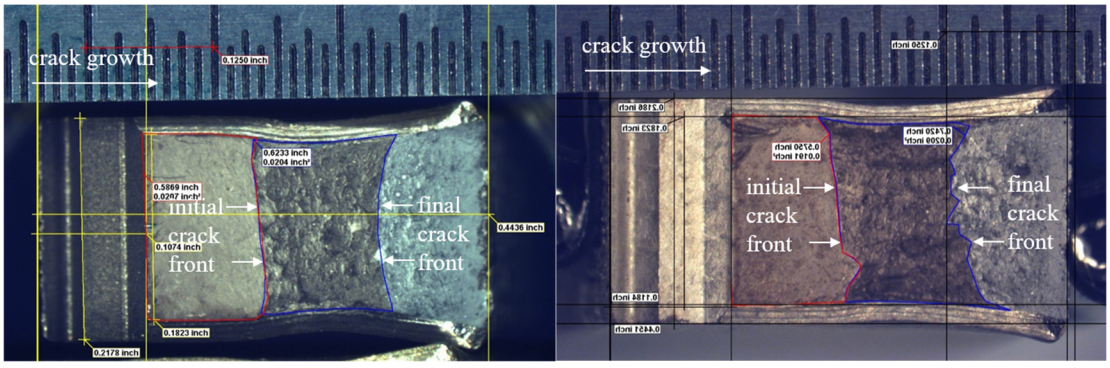

(a) (b)

Figure 5. The fracture surfaces of the (a) TS-2 specimen and (b) TS-4 specimen.

3. 2-D FE Analyses with CZM

3.1 2-D Plane Strain FE Models of Full Bend Specimens

As mentioned earlier, 2-D plane strain FE analyses with the nodal release method are first conducted to simulate crack extensions in the uncharged and hydrogen-charged LS and TS bend specimens with finite-step crack extensions to obtain the initial estimates of the changing cohesive parameters. The 2-D plane strain FE analyses with the nodal release method are presented in Appendix A. In this section, 2-D plane strain FE analyses with cohesive elements for the uncharged and hydrogen-charged LS and TS bend specimens are presented. Figure 6 shows the FE model for the uncharged LS-2 bend specimen with cohesive elements. The Cartesian $X-Y$ coordinate system is also shown in Figure 6. In the figure, the loading pin and the supporting pins have the same radius of 3.175 mm and are modeled as analytical rigid bodies. The interfaces between the pins and bend specimens are modeled with the contact definition of no-penetration in the normal direction and frictionless in the tangential direction. For the boundary conditions, the supporting pins are fixed, and a downward displacement is applied to the loading pin. The cohesive elements are placed directly ahead of the initial crack tip in the Y direction marked in blue as shown in Figure 6. In order to avoid excess overlap in the severely compressive region and constrain the rigid body motion in the X direction, the X -symmetry boundary condition is applied to a small portion of the crack paths (about 0.5 mm) near the upper surface of the specimen, marked in yellow in Figure 6. The FE models for the other three cases are similar to the one in Figure 6 and will not be shown here.

The detailed design of the notches for mounting the clip gauge for measuring the CMOD is not modeled since the region near the mounting notches hardly deforms. However, computational displacements are still collected for the CMOD from the locations of two notch

tips shown in Figure 6. The locations to take the initial CMOD are marked as red dots in Figure 6. The computational initial CMOD is 2.6 mm, slightly larger than the experimental value of 2.54 mm. 2-D plane strain linear elements with full integration (CPE4) are used. Three element sizes of 0.1 mm by 0.1 mm, 0.2 mm by 0.2 mm and 0.4 mm by 0.4 mm are used in the finite element model. The smallest elements of 0.1 mm by 0.1 mm are located near the crack and the cohesive elements, and near the contact surfaces. The smallest element size is selected in the order of the crack tip opening displacement to catch the maximum opening stresses ahead of the crack tips.

The material definitions for the uncharged AM 304 stainless steel in the LS and TS orientations were obtained from tensile test results as presented in Sung et al. (2019). The Young's modulus E is determined to be 190 GPa, the Poisson's ratio ν is assumed to be 0.3, and the yield stress σ_0 is determined to be 290 MPa for the uncharged AM 304 stainless steels in the LS orientation. The Young's modulus E is determined to be 176 GPa, the Poisson's ratio ν is assumed to be 0.3, and the yield stress σ_0 is determined to be 347 MPa for the uncharged AM 304 stainless steels in the TS orientation. Table 2 lists the values of the Young's modulus E, Poisson's ratio ν, and the yield stress σ_0 for the uncharged AM 304 stainless steels in the LS and TS orientations. The initial parts of the true stress-plastic strain curves are determined from the experimental engineering stress-strain curves up to the strains corresponding to the maximum engineering stresses. The final parts of the true stress-plastic strain curves are based on a power-law relation to extend the initial experimental curves as

$$\sigma = \sigma_0 + k\left(\varepsilon_p\right)^n \tag{2}$$

where σ is the true stress, σ_0 is the yield stress, ε_p is the plastic strain and k and n are

material constants. Figure 7 shows the input true stress-plastic strain curves for the uncharged LS and TS specimens as presented in Sung et al. (2019). Table 2 also lists the values of k and n for the uncharged AM 304 stainless steels in the LS and TS orientations. It should be pointed out that the initial part of the true stress-plastic strain curve for the TS tensile specimen is slightly higher than that of the LS tensile specimen. However, the hardening exponent n of the fitted true stress-plastic strain curves for the TS tensile specimen is lower compared with that of the LS tensile specimen. The same material definitions and same input true stress-plastic strain curves of the uncharged LS and TS specimens are used for the corresponding hydrogen-charged LS and TS specimens, respectively, due to lack of the corresponding tensile test results. For cohesive elements, the PPR user-defined cohesive element subroutine (Park et al. 2009; Park and Paulino 2012) for ABAQUS is adopted but with the use of the smooth trapezoidal TSL (Cornec et al. 2003). The commercial finite element program ABAQUS was employed to perform the analyses of the LS and TS bend specimens with consideration of geometric nonlinearity.

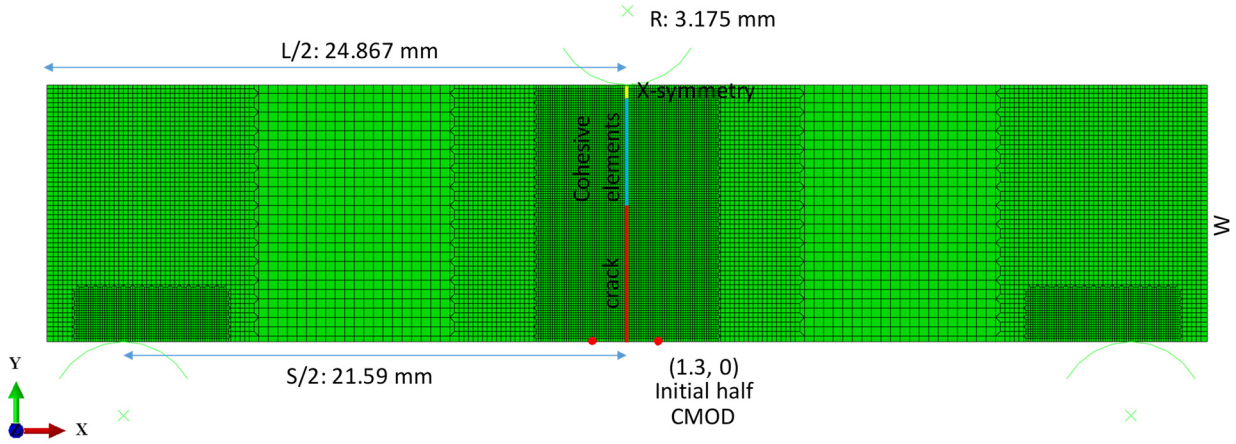

Figure 6. The FE model of the LS-2 specimen.

Table 2. The Young's modulus E, the Poisson's ratio ν, the yield stress σ_0, and the material constants k and n for the LS and TS tensile specimens.

Specimen	Young's modulus E (GPa)	Poisson's ratio ν	Yield stress σ_0 (MPa)	k	n
LS	190	0.3	290	1248.17	0.7
TS	176	0.3	347	1123.18	0.63

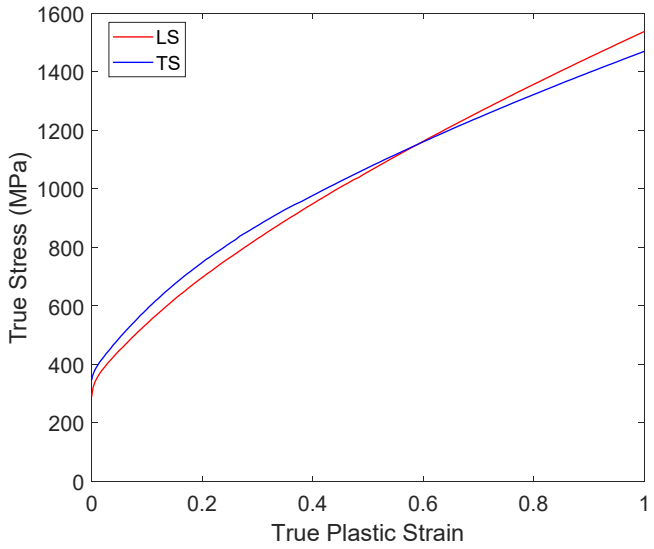

Figure 7. The true stress-plastic strain curves for the bend specimens in the LS and TS orientations.

3.2 Cohesive Zone Modeling

The CZM approach is adopted to model the crack extensions in the uncharged and hydrogen-charged LS and TS bend specimens in this investigation. Cohesive elements with zero thickness are inserted along the prescribed crack path between the regular continuum elements to model the interfacial mechanical behavior in the normal direction. Various TSLs and frameworks of cohesive elements were developed for different applications. The smooth trapezoidal TSL (Cornec et al. 2003; Scheider and Brocks 2003, 2006; Sung et al. 2019; Wu et al. 2020, 2021) was selected to simulate crack extensions in FE analyses of fracture specimens of ductile metals. The smooth trapezoidal TSL has the initial stiff part so that the initial responses

of the experimental load-displacement curves of fracture specimens can be fitted well to check the accuracies of the FE analyses (Cornec et al. 2003; Scheider and Brocks 2003, 2006; Sung et al. 2019; Wu et al. 2020, 2021). Figure 8 shows a schematic of the normalized smooth trapezoidal TSL. The smooth trapezoidal TSL expresses the traction T as a piecewise function in terms of the separation δ as

$$T = \begin{cases} T_0\left[2\left(\dfrac{\delta}{\delta_1}\right)-\left(\dfrac{\delta}{\delta_1}\right)^2\right] & 0 \le \delta < \delta_1 \\ T_0 & \delta_1 \le \delta < \delta_2 \\ T_0\left[2\left(\dfrac{\delta-\delta_2}{\delta_0-\delta_2}\right)^3-3\left(\dfrac{\delta-\delta_2}{\delta_0-\delta_2}\right)^2+1\right] & \delta_2 \le \delta < \delta_0 \end{cases} \tag{3}$$

In Equation (3), T_0 is the cohesive strength. Here, δ_1 and δ_2 are the beginning and end separations of the constant cohesive strength portion as shown in Figure 8. δ_0 is the failure separation of the cohesive elements. The area under the TSL curve is defined as the cohesive energy Γ_0. It should be noted that δ_1 should be small enough to prevent inducing too much artificial compliance for the fracture specimens as mentioned earlier but large enough to assure computational stability. In this investigation, the ratio δ_1/δ_0 is selected to be 0.005 for all simulations. Since the remaining ligament of a bend specimen is mainly subjected to bending, the upper part of the ligament is under compression. For $\delta < 0$, an elastic response with a large stiffness (500 times of the initial tensile stiffness) is assigned to prevent significant overlap of two adjacent continuum elements.

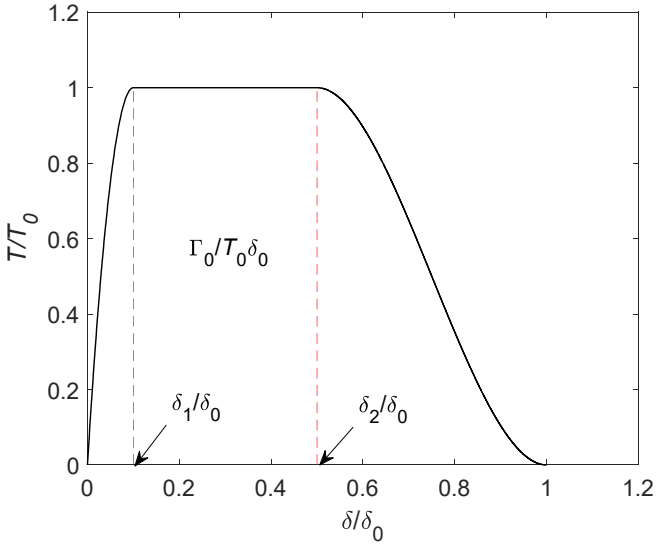

Figure 8. The normalized TSL with a smooth trapezoidal shape.

4. Selection of Changing Cohesive Parameters and Simulation Results

2-D plane strain FE analyses to simulate crack extensions by nodal release are first conducted. The procedures of the 2-D FE analyses to simulate crack extensions by nodal release for the bend specimens are similar to those for arc-shaped tension specimens in Sung et al. (2021a) and are presented in Appendix A. The simulation results presented in Appendix A indicate that the near-tip maximum opening stresses and separation work rates change with increasing crack extension. These suggest that T_0 and Γ_0 may change with increasing crack extension.

In this investigation, the calibration procedure of Wu et al. (2021) is adopted. The detailed calibration steps were presented in Wu et al. (2021) and briefly summarized here. In the first step, the Γ_0 and T_0 increase with increasing crack extension to fit the experimental displacement and crack extension corresponding to the experimental maximum load. In the second step, the Γ_0 and T_0 decrease with increasing crack extension to fit the slope of the

experimental load vs crack extension curve. The general trends of the increasing and decreasing Γ_0 and T_0 as functions of the crack extension are similar to those of the separation work rate vs crack extension and near-tip maximum opening stress vs crack extension curves, respectively, as presented in Appendix A. In other words, the stress-state dependency and the 3-D thickness effects enter into the TSL through the changing T_0 and Γ_0 based on the trends of the near-tip maximum opening stress and separation work rate obtained from the nodal release method. In this investigation, the softening ratios δ_2/δ_0 's are kept as constant values of 0.22 for the LS-2 specimen and 0.3 for the LS-4, TS-2 and TS-4 specimens for numerical stability as specified and discussed in Sung et al. (2019).

Figures 9, 10, 11 and 12 show that T_0 's and Γ_0 's increase and then decrease with increasing distance to the initial crack tip for the LS-2, LS-4, TS-2 and TS-4 specimen, respectively. The constant T_0 's and constant Γ_0 's selected in Sung et al. (2019) for the LS-2, LS-4, TS-2 and TS-4 specimen are also shown in the figures. The discussion of the hydrogen effects on the constant T_0 and Γ_0 can be found in Sung et al. (2019). The hydrogen effects on the changing T_0 and Γ_0 can be observed in Figures 9, 10, 11, and 12. As shown in Figures 9 and 10, the LS-4 specimen has the lower changing T_0 and Γ_0 curves than those of the LS-2 specimen. As shown in Figures 11 and 12, the TS-4 specimen has the lower changing T_0 but similar Γ_0 curves compared with those of the TS-2 specimen. It should be mentioned again that the general trends of the changing T_0 's and Γ_0 's for the LS-2, LS-4, TS-2 and TS-4 specimens are based on the general trends of the changing near-tip maximum opening stresses and separation work rates from the 2-D FE analyses to simulate crack extensions by nodal release as discussed in Appendix A.

As shown in Figures 9, 10, 11, 12, A5 and A6, there are two stages for the crack extensions in these sub-sized bend specimens. In the first stage, the crack extension starts from near plane strain conditions and gradually approaches to the plane stress conditions due to the extensive plastic deformations and the necking as shown in Figures 4 and 5. Therefore, the near-tip maximum opening stress and separation work rate, and T_0 and Γ_0 increase as the crack extension increases in the first stage as shown in Woelke et al. (2015) and Andersen et al. (2019). In the second stage, the near-tip maximum opening stress and separation work rate, and T_0 and Γ_0 remain constants and then slightly decrease as the crack extension increases possibly due to the decrease of the remaining ligament and the large drop of the specimen load.

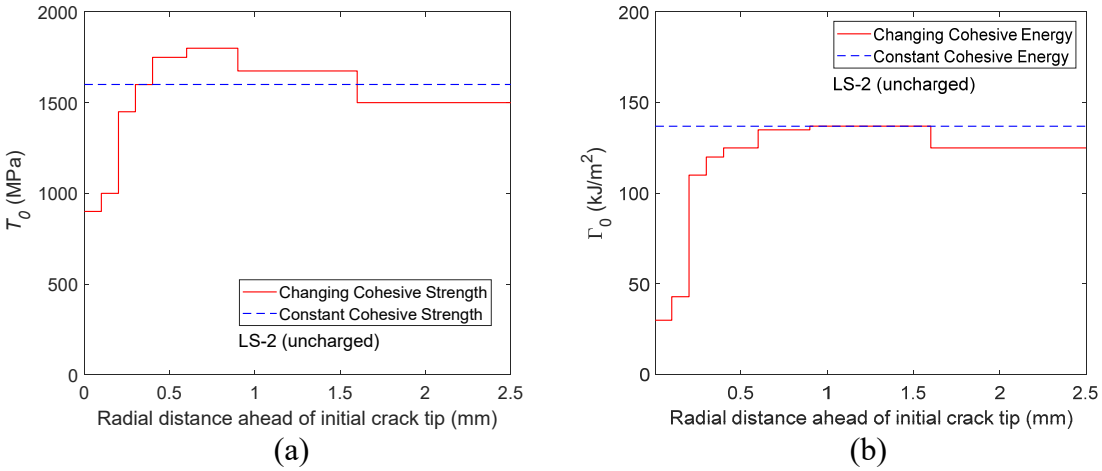

Figure 9. (a) The changing T_0 and (b) the changing Γ_0 for the LS-2 specimen.

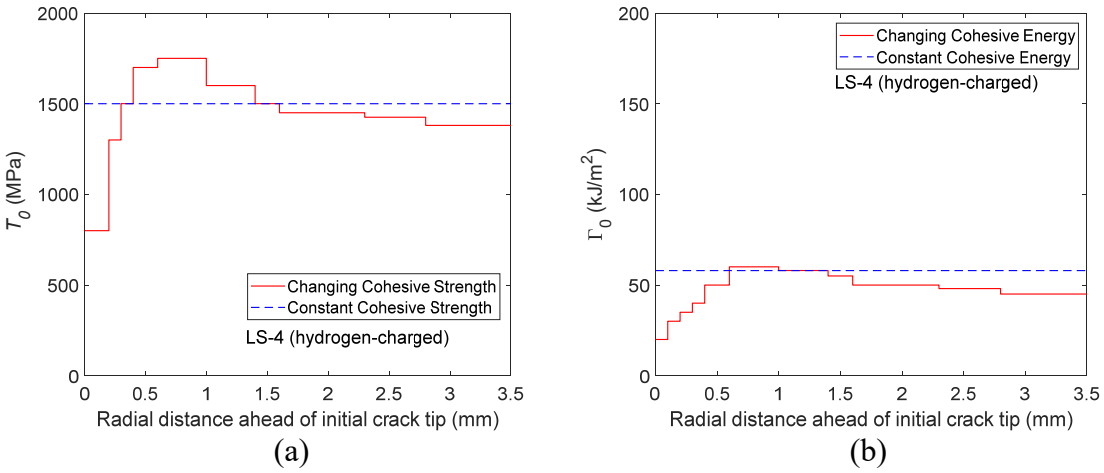

Figure 10. (a) The changing T_0 and (b) the changing Γ_0 for the LS-4 specimen.

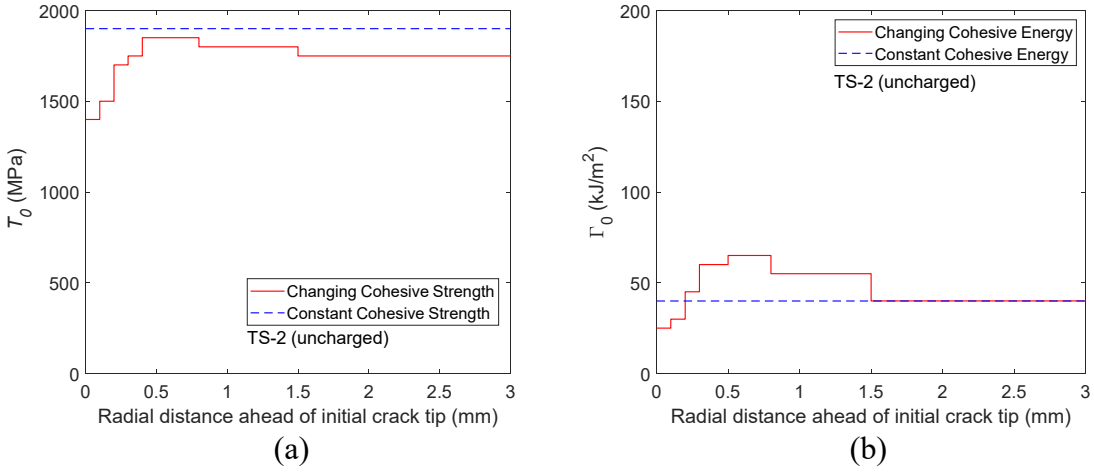

Figure 11. (a) The changing T_0 and (b) the changing Γ_0 for the TS-2 specimen.

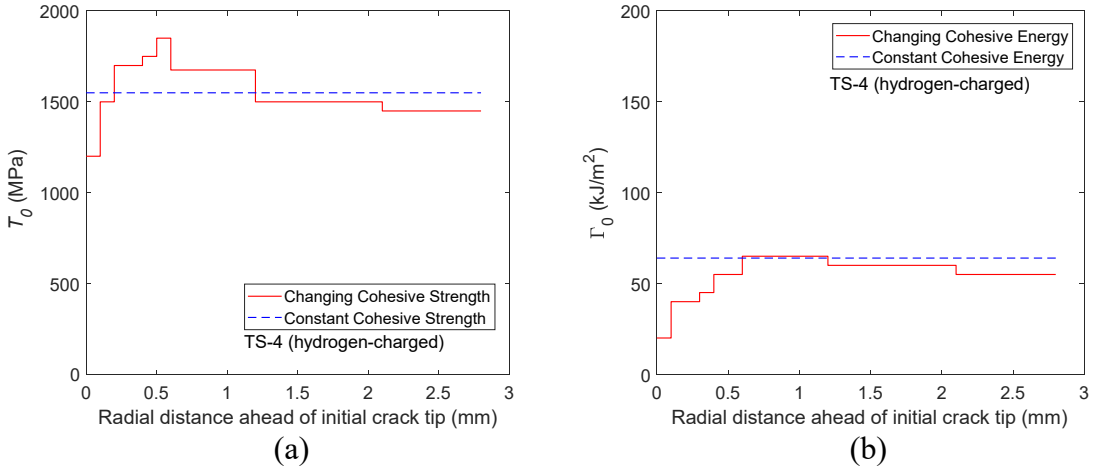

Figure 12. (a) The changing T_0 and (b) the changing Γ_0 for the TS-4 specimen.

The simulation results with the changing T_0's and Γ_0's for the LS-2, LS-4, TS-2 and TS-4 specimens are presented and compared with the test results in Figures 13, 14, 15, and 16 respectively. The simulation results with the constant T_0's and Γ_0's in Sung et al. (2019) are also shown in the figures. As shown in Figures 13, 14, 15, and 16, the simulation results with the constant T_0's and Γ_0's in Sung et al. (2019) can only match the general trends of the test results. The simulation results with the changing T_0's and Γ_0's can match well with the entire test results for the LS-2, LS-4, TS-2, and TS-4 specimens. For example, Figures 13(a), 13(b), 14(a), 14(b), 15(a), 15(b), 16(a) and 16(b) show that the simulation CMODs and crack extensions (Δa) with the changing T_0's and Γ_0's corresponding to the simulation maximum loads can match well with the test results. The simulation CMODs and Δa with the constant T_0's and Γ_0's corresponding to the simulation maximum loads are smaller than the test results. This suggests the lower cohesive energies should be selected for the initial part of crack extensions. Also, Figures 13(b), 14(b), 15(b), and 16(b) show that the simulation load (P) and its slope of the simulation P vs Δa curve with the changing T_0's and Γ_0's for the entire crack growth can match well with the test results.

In order to compare the selected constant cohesive parameters in Sung et al. (2019) and the changing cohesive parameters selected in this investigation, the average cohesive strength $\overline{T}_0$ and the average cohesive energy $\overline{\Gamma}_0$ defined in Wu et al. (2021) are adopted here. According to Wu et al. (2021), $\overline{T}_0$ and $\overline{\Gamma}_0$ are defined as

$$\overline{T}_0 = \frac{\int T_0 \mathrm{d}(\Delta a)}{\Delta a_f} \tag{4}$$

and

$$\overline{\Gamma}_0 = \frac{\int \Gamma_0 \mathrm{d}(\Delta a)}{\Delta a_f} \tag{5}$$

where Δa represents the crack extension and Δa_f represents the final crack extension measured from the experiment. The values of the average cohesive strength $\overline{T}_0$ and cohesive energy $\overline{\Gamma}_0$ of the changing cohesive parameters and the values of the constant cohesive strength T_0 and cohesive energy Γ_0 in Sung et al. (2019) for the uncharged LS-2 and the hydrogen-charged LS-4 specimens are listed in Table 3. The values of the average cohesive strength $\overline{T}_0$ and cohesive energy $\overline{\Gamma}_0$ of the changing cohesive parameters and the values of the constant cohesive strength T_0 and cohesive energy Γ_0 in Sung et al. (2019) for the uncharged TS-2 and the hydrogen-charged TS-4 specimens are listed in Table 4. As listed in Tables 3 and 4, the values of the average cohesive strength $\overline{T}_0$ and cohesive energy $\overline{\Gamma}_0$ of the changing cohesive parameters in this investigations are close to those of the constant cohesive strength T_0 and cohesive energy Γ_0 in Sung et al. (2019), respectively. This suggests that the general trends of the computational load-displacement, load-crack extension, crack extension-displacement, and J-R curves can be obtained by using the average cohesive strength $\overline{T}_0$ and cohesive energy $\overline{\Gamma}_0$ in this investigation or the constant cohesive strength T_0 and cohesive energy Γ_0 in Sung et al. (2019).

As listed in Tables 3 and 4, the average cohesive strengths $\overline{T}_0$'s of the uncharged specimens are higher than those of the hydrogen-charged specimens for both the LS and TS specimens. The average cohesive energies $\overline{\Gamma}_0$'s of the uncharged specimens are either higher or slightly lower than those of the hydrogen-charged specimens. Tables 3 and 4 also indicate that the cohesive strengths T_0's and $\overline{T}_0$'s of the uncharged and hydrogen-charged LS specimens are

lower than those of the uncharged and hydrogen-charged TS specimens, respectively. The cohesive energies Γ_0 and $\overline{\Gamma}_0$ of the uncharged LS specimen are higher than those of the uncharged TS specimen. The cohesive energies Γ_0 and $\overline{\Gamma}_0$ of the hydrogen-charged LS specimen are lower than those of the hydrogen-charged TS specimen.

Table 3. A comparison of the constant cohesive parameters of the constant cohesive parameter approach and the average cohesive parameters of the changing cohesive parameter approach for the LS-2 and LS-4 specimens.

	Approach	T_0 or $\overline{T}_0$ (MPa)	Γ_0 or $\overline{\Gamma}_0$ (kJ/m^2)
LS-2 (uncharged)	Constant	1,600	137
	Changing (average)	1,563	121.7
LS-4 (hydrogen-charged)	Constant	1,500	58
	Changing (average)	1,461	48.9

Table 4. A comparison of the constant cohesive parameters of the constant cohesive parameter approach and the average cohesive parameters of the changing cohesive parameter approach for the TS-2 and TS-4 specimens.

	Approach	T_0 or $\overline{T}_0$ (MPa)	Γ_0 or $\overline{\Gamma}_0$ (kJ/m^2)
TS-2 (uncharged)	Constant	1,900	40
	Changing (average)	1,754	46.67
TS-4 (hydrogen-charged)	Constant	1,550	64
	Changing (average)	1,550	56.1

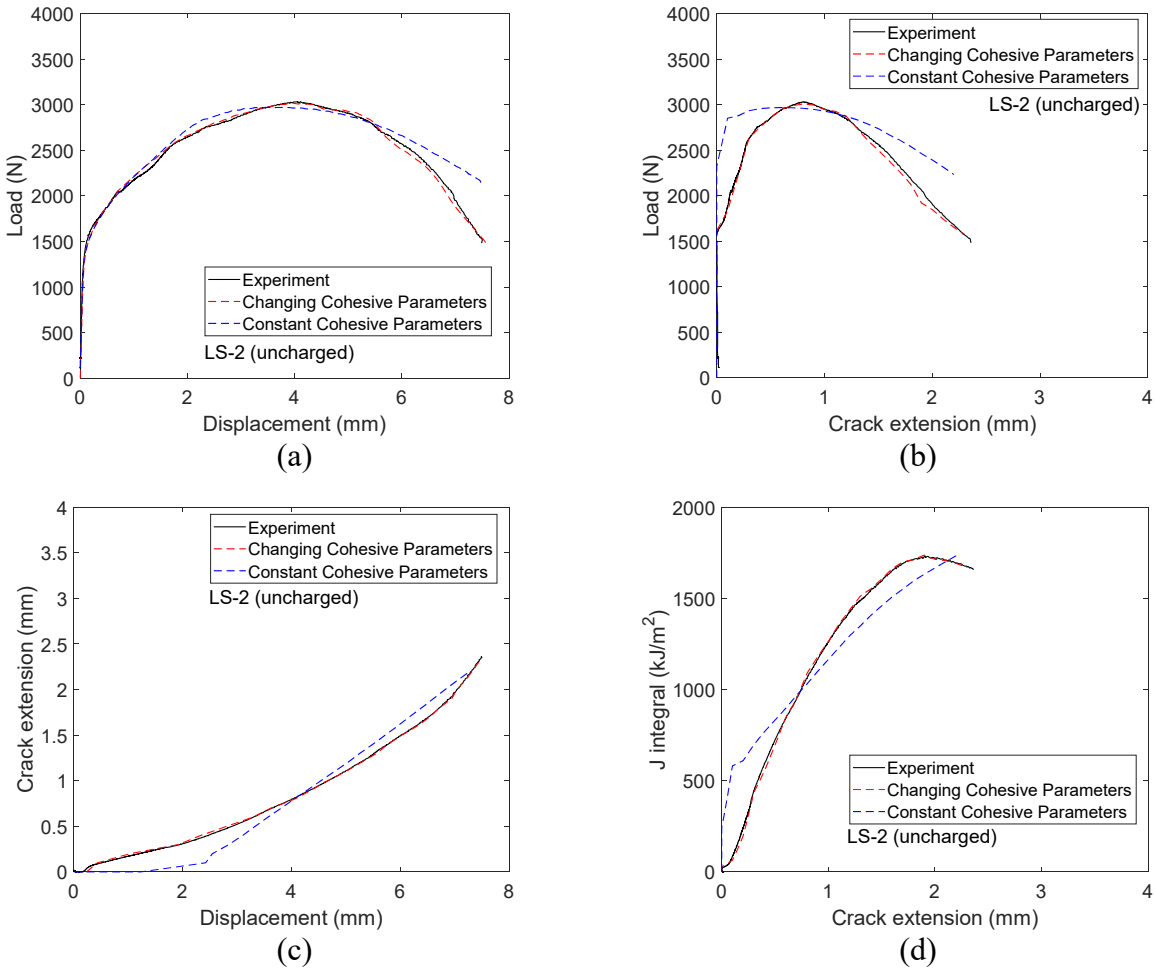

Figure 13. The simulation results with the changing T_0 and Γ_0 in this investigation, the simulation results with the constant T_0 and Γ_0 (Sung et al. 2019), and the test results for the LS-2 specimen.

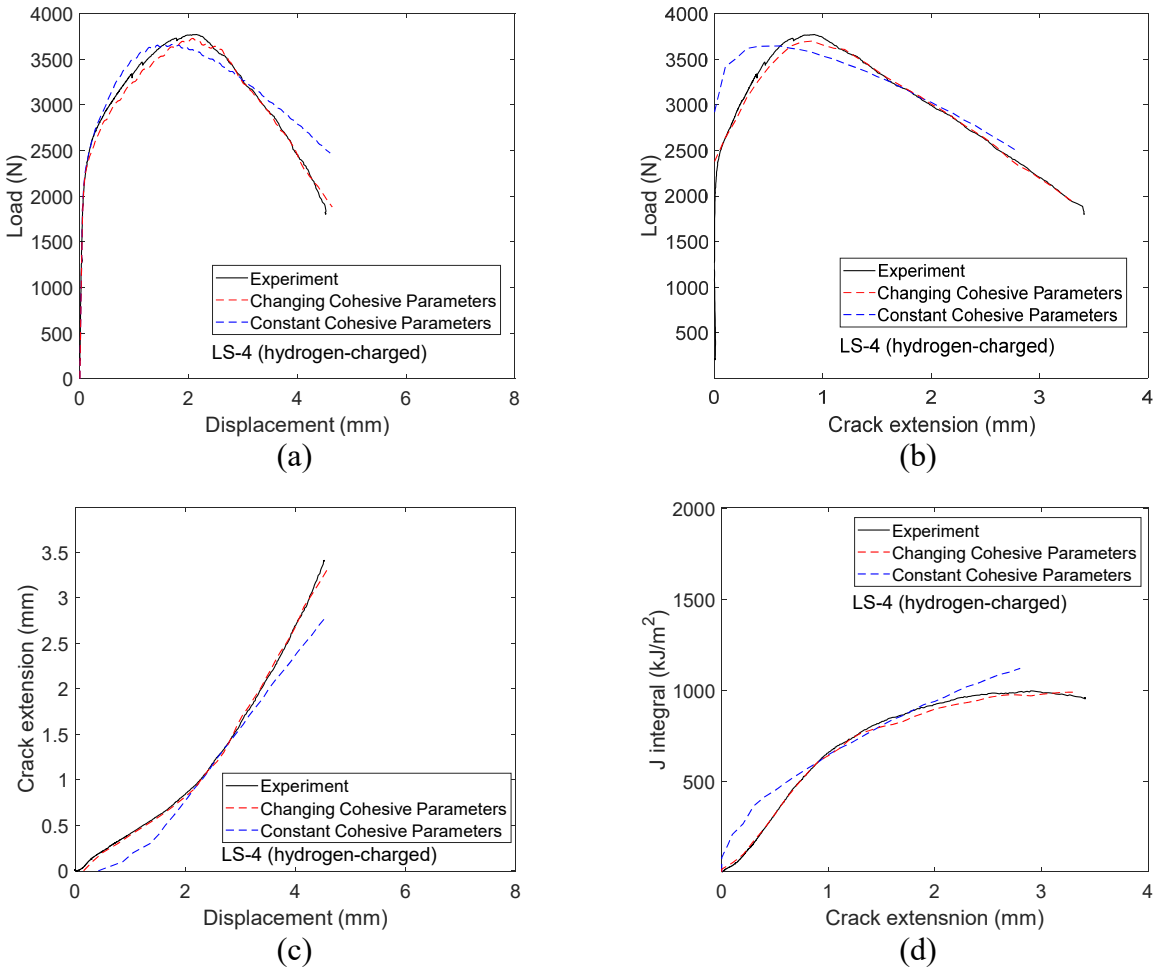

Figure 14. The simulation results with the changing T_0 and Γ_0 in this investigation, the simulation results with the constant T_0 and Γ_0 (Sung et al. 2019), and the test results for the LS-4 specimen.

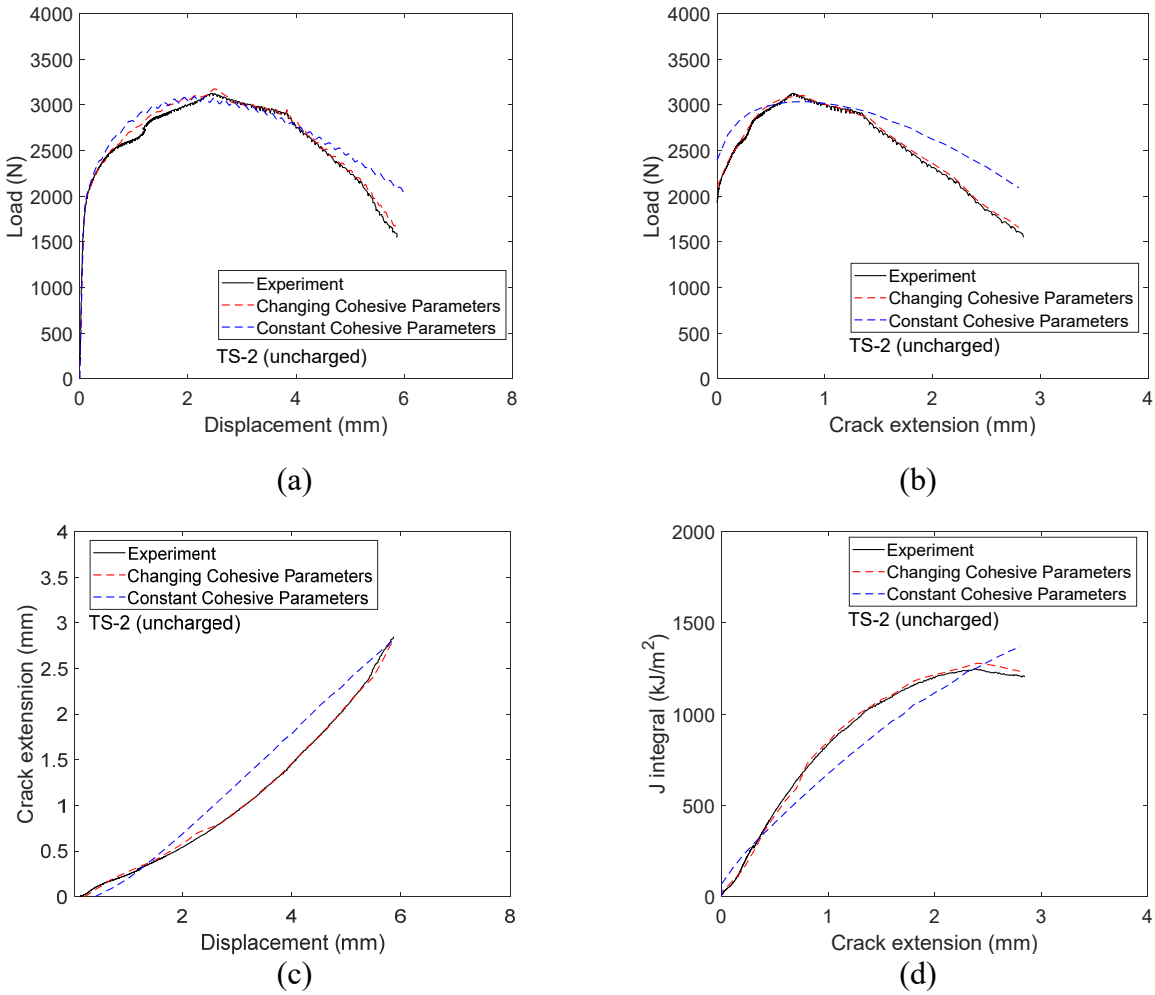

Figure 15. The simulation results with the changing T_0 and Γ_0 in this investigation, the simulation results with the constant T_0 and Γ_0 (Sung et al. 2019), and the test results for the TS-2 specimen.

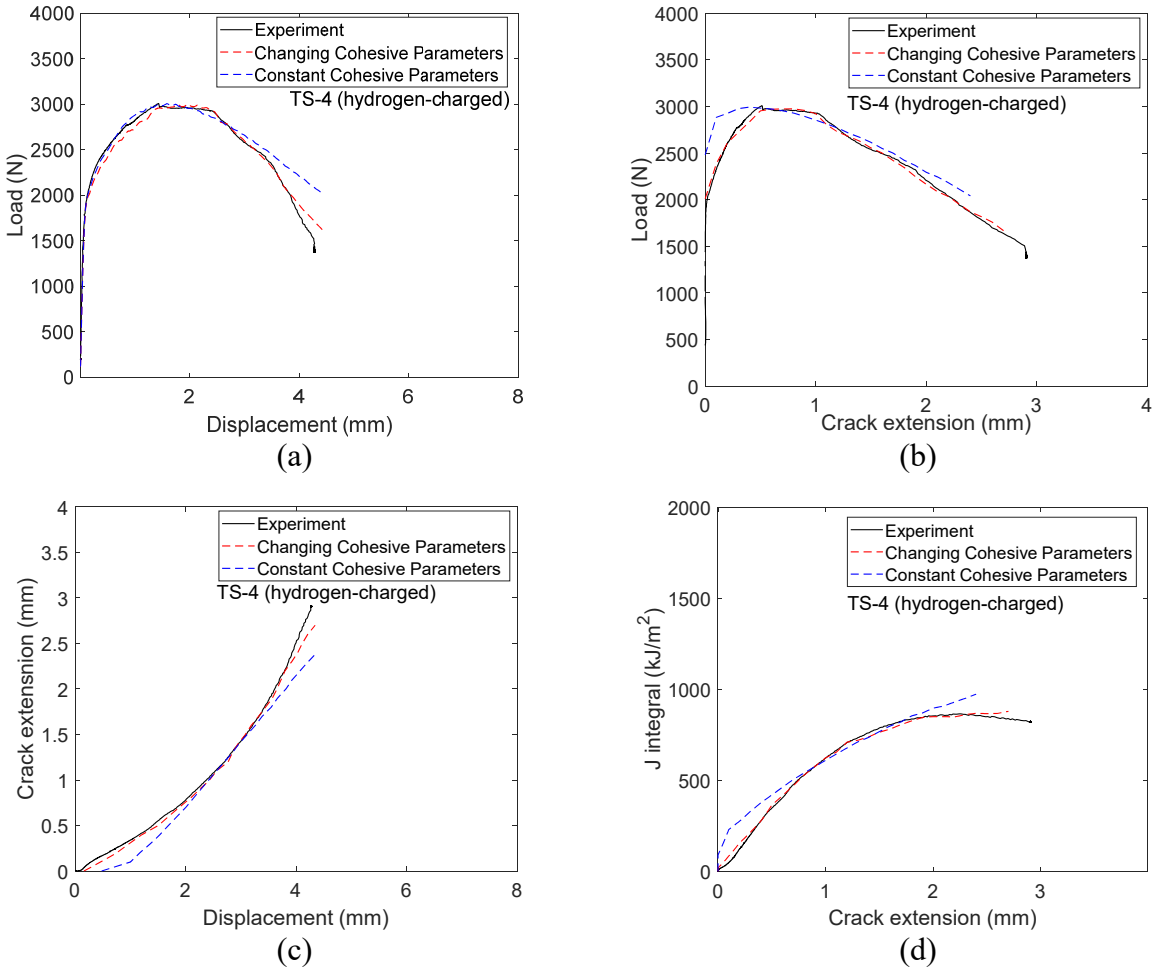

Figure 16. The simulation results with the changing T_0 and Γ_0 in this investigation, the simulation results with the constant T_0 and Γ_0 (Sung et al. 2019), and the test results for the TS-4 specimen.

5. Simulation Results from a 3D FE Analysis

As indicated in Appendix A, the increasing and decreasing stress triaxiality with increasing crack extension in bend specimens cannot be used to explain the calibrated increasing and decreasing cohesive energies with increasing crack extension from the 2-D plane strain FE analyses. However, the increasing and decreasing separation work rates from the energy balance viewpoint based on the test results are consistent with the increasing and decreasing cohesive energies with increasing crack extension from the 2-D plane strain FE analyses. Therefore, a 3-D FE analysis of one bend specimen is conducted to examine the plane strain conditions in the thickness direction with increasing crack extension.

In this investigation, a 3-D FE analysis to simulate crack extensions by nodal release is performed for the LS-2 specimen. A schematic of the full side-grooved LS-2 specimen is shown in Figure 17(a). Due to symmetry, only the left back quarter of the bend specimen is selected to model as indicated in the figure. The 3-D FE model of the left back quarter of the bend specimen is shown in Figure 17(b). The front surface marked in green represents the Z-symmetry condition and the right surface marked in blue represents the X-symmetry condition as shown in Figure 17(b). The crack is marked in red and the back side groove is shown on the right part of the right surface. The crack length of 5.939 mm and the remaining ligament length of 5.059 mm are also marked in the figure.

Figure 18(a) shows the front view of the FE model with five partitions of different mesh sizes. Figure 18(a) also shows the tie constraints marked as green lines used to impose the displacement continuity conditions between the regions of different element sizes. The smallest elements near the crack plane have the size of 0.1 mm by 0.1 mm by 0.1 mm. Figure 18(b) shows the top view of the FE model. It should be mentioned that the depth of the side groove is

0.476 mm and side groove angle is set at 45 degrees. Figure 18(c) shows the right view of the FE model with four defined paths on the crack plane. As shown in Figure 18(c), Path 1 is at the center plane (mid-section) of the specimen, Path 2 is at the quarter plane of the specimen, Path 3 is four elements away from the side groove front and Path 4 is only one element away from the side groove front. In the 3-D FE model, the crack front is assumed to be extended uniformly to follow the test results as shown in Figure A2(a). The nodal release procedures in the 3-D FE analysis are similar to those in Sung et al. (2021b) and will not be presented in detail here.

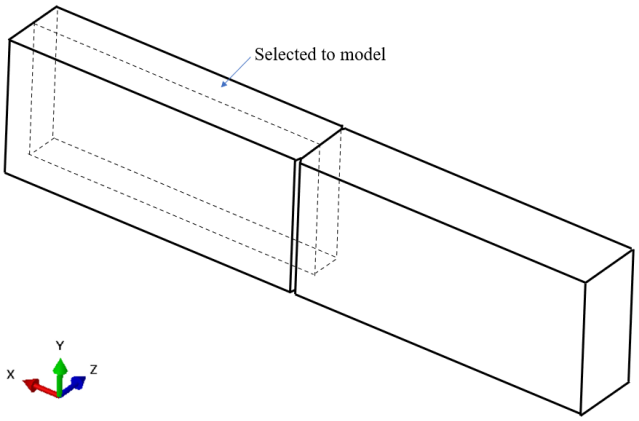

(a)

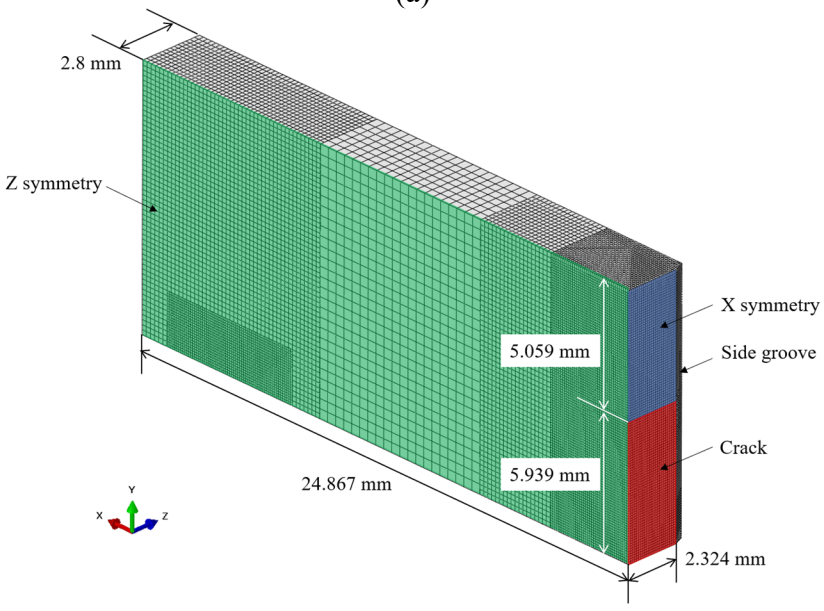

(b)

Figure 17. (a) A schematic of the full side-grooved LS-2 specimen and (b) the 3-D FE model of the left back quarter of the LS-2 specimen.

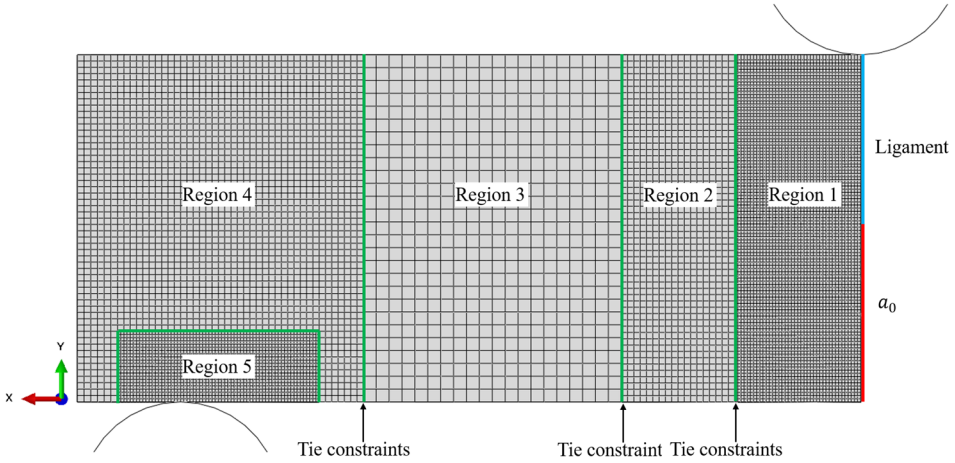

(a)

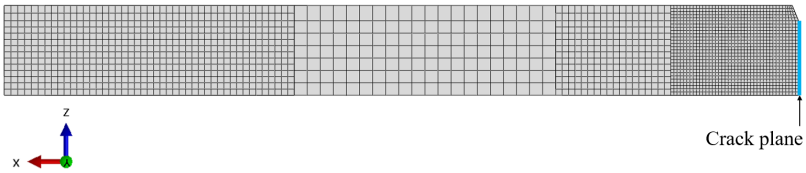

(b)

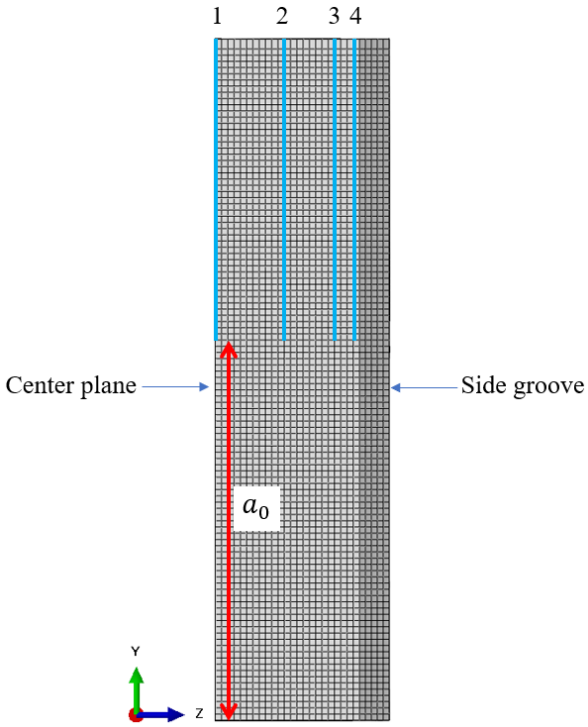

(c)

Figure 18. (a) The front view of the FE model with partitions of different mesh sizes, (b) the top view of the FE model showing the depth and angle of the side-groove, and (c) the right view of the FE model with four defined paths on the crack plane.

Figure 19 shows the opening stresses σ_{xx}'s and the near-tip maximum opening stresses with increasing crack extension along Paths 1 to 4 as defined in Figure 18(c). In these figures, the black dotted lines represent the σ_{xx} distributions in front of the growing crack fronts at the ends of crack extension steps and the red solid lines represent the connections of the near-tip maximum opening stress locations in front of the growing crack fronts. As shown in Figure 19(a), the near-tip maximum opening stresses along Path 1 (center plane) increase with the values of 1,038 MPa to 1,871 MPa during the crack extension and then decrease. Similar increases and decreases of the near-tip maximum opening stresses along Paths 2 to 4 are also observed in Figures 19(b) to 19(d). The increases and decreases of the near-tip maximum opening stresses along Paths 1 to 4 are similar to the results from the 2-D plane strain FE analysis as shown in Figure A5(a). As shown in Figures 19(a) to 19(d), the element size is small enough to be able to catch the increases of the opening stresses to the maximum values as the radial distances to the crack fronts increase along Paths 1 to 4. As also shown in Figure 19, the near-tip maximum opening stresses are slightly higher along Paths 2 and 3, and the near-tip maximum opening stresses are noticeably lower along Path 4 near the side groove front.

Figure 20 shows the out-of-plane stresses σ_{zz}'s in the Z direction in front of the growing crack fronts during the crack extension along Paths 1 to 4 as defined in Figure 18(c). In these figures, the black dotted lines represent the σ_{zz} distributions in front of the growing crack fronts at the ends of crack extension steps and the red solid lines represent the connections of the near-tip maximum out-of-plane stress locations in front of the growing crack fronts. Because the out-of-plane stresses are much lower along Path 4 (near surface) and relatively lower along Path 3, compared with those along Path 1 (center plane) and Path 2 (quarter plane), the plane strain conditions are not satisfied near the side grooves with increasing crack extension. The loss of

the plane strain conditions in the thickness direction may be the reason for the increase of Γ_0 with increasing crack extension.

Figure 21 shows the stress triaxialities α's in front of the growing crack fronts during the crack extension along Paths 1 to 4 as defined in Figure 18(c). The stress triaxiality α is defined as the ratio of the hydrostatic tension to the tensile effective stress. In these figures, the black dotted lines represent the α distributions in front of the growing crack fronts at the ends of crack extension steps and the red solid lines represent the connections of the maximum stress triaxiality locations in front of the growing crack fronts. The simulation results indicate that the maximum values of α in front of the growing crack fronts increase, decrease and increase with the values from 2.23 to 3.20, from 2.14 to 2.57, and from 1.92 to 1.64 along Path 1 (center plane), Path 2 (quarter plane), and Path 3 (four elements away from the side groove front), respectively. But the values decrease and increase from 1.58 to 1.33 along Path 4 (one element away from the side groove front). The lower maximum stress triaxialities along Path 2, Path 3 and Path 4 suggest again that the loss of the constraint conditions or plane strain conditions in the thickness direction with increasing crack extension. It should be pointed out that the maximum values of α along Path 1 (center plane) in the 3-D FE analysis shown in Figure 21(a) are smaller than those in the 2-D FE analysis as shown in Figure A7(a). Also, Figure 21(a) shows a decrease part of the maximum values of α for crack extension less than 1 mm along Path 1 (center plane) in the 3-D FE analysis, which cannot be observed in Figure A7(a) for those in the 2-D FE analysis. It should be noted that Siegmund and Brocks (2000a) indicated that the cohesive energy increases as the stress triaxiality decreases based on the Gurson material model for ductile fracture. The loss of the plane strain conditions in the thickness direction toward to the plane stress conditions with increasing crack extension may be the dominant factor for the increase of

the separation work rate or Γ_0 based on the results of the 2-D and 3-D FE analyses to simulate crack extensions.

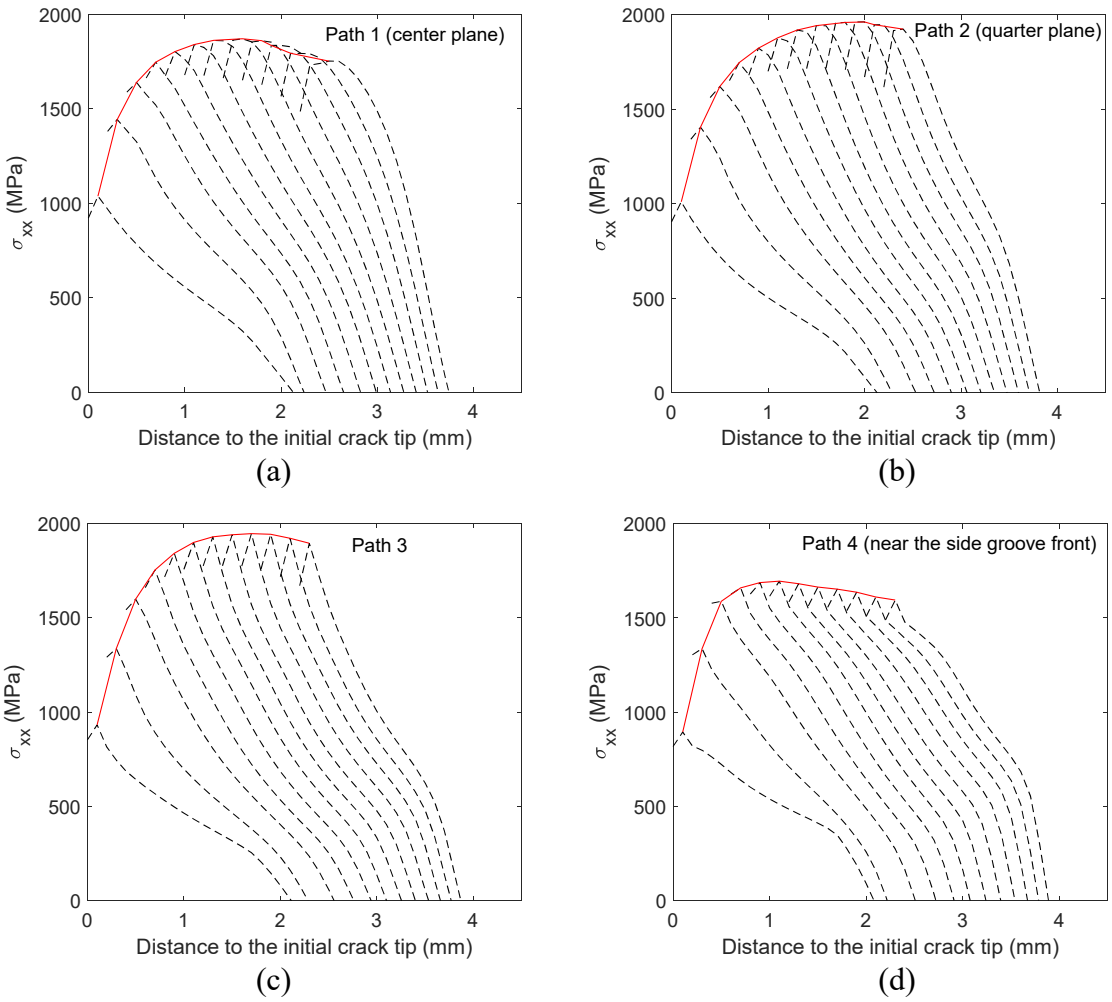

Figure 19. The opening stresses and near-tip maximum opening stresses along (a) Path 1 (center plane), (b) Path 2 (quarter plane), (c) Path 3 and (d) Path 4 (near the side groove front) for the LS-2 specimen.

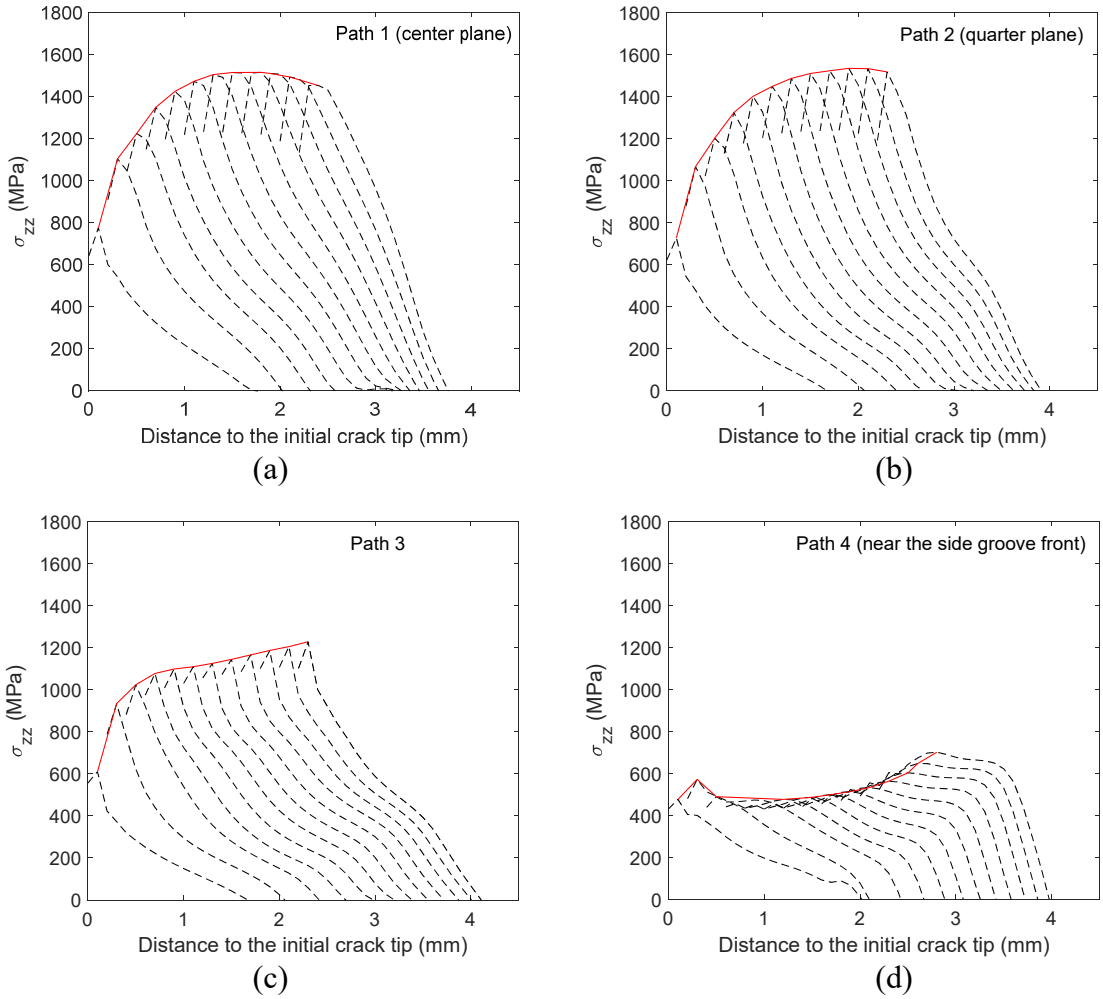

Figure 20. The near-tip out-of-plane stresses along (a) Path 1 (center plane), (b) Path 2 (quarter plane), (c) Path 3 and (d) Path 4 (near the side groove front) for the LS-2 specimen.

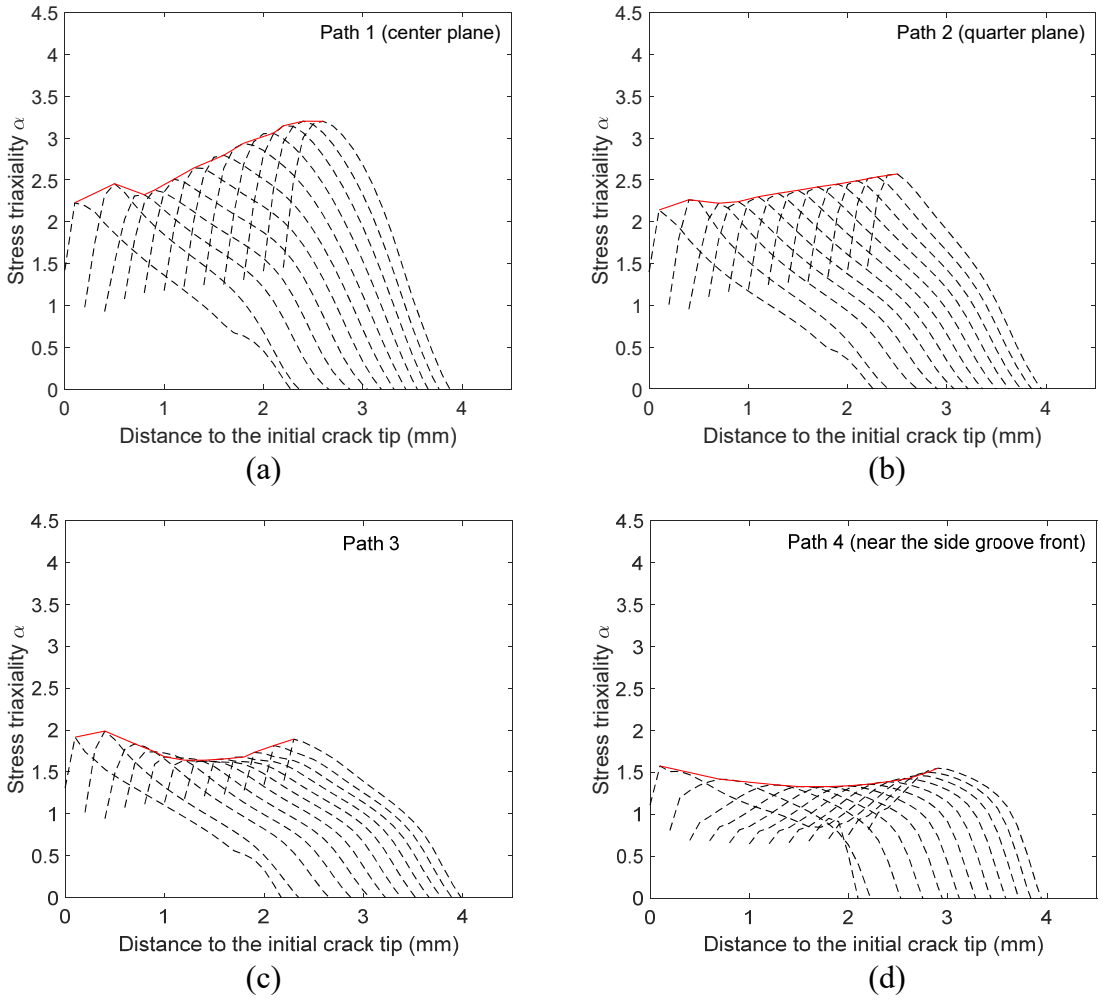

Figure 21. The stress triaxialities along (a) Path 1 (center plane), (b) Path 2 (quarter plane), (c) Path 3 and (d) Path 4 (near the side groove front) for the LS-2 specimen.

Figure 22 shows the fracture surface at the end of the 3-D FE simulation for the LS-2 specimen. The necking part of the LS-2 specimen from the simulation results is remarkably similar to the experimental observation as shown in Figure 4(a). The necking parts of the bend specimens shown in Figures 4 and 5 suggest the transition of the stress states in the thickness direction to near plane stress states with increasing crack extension. With the transition to the plane stress states, the separation work rates or Γ_0's should increase even with the side grooves to promote the flat fracture mode with increasing crack extension, as suggested by the simulation results of Woelke et al. (2015) for the initial part of the crack growth in a large thin cracked

specimen. The final decrease portions of the separation work rates or Γ_0's may be related to the large drops of the specimen loads and the increases of the out-of-plane stresses near the side groove fronts or the increases of stress triaxialities with increasing crack extension under the fully yielded conditions with small ligaments. Therefore, the Γ_0's in the simplified 2-D plane strain FE analyses with the CZM approach should change to account for the constraint condition change in the thickness direction as the changing separation work rates to model the 3-D crack extensions in these sub-sized bend specimens.

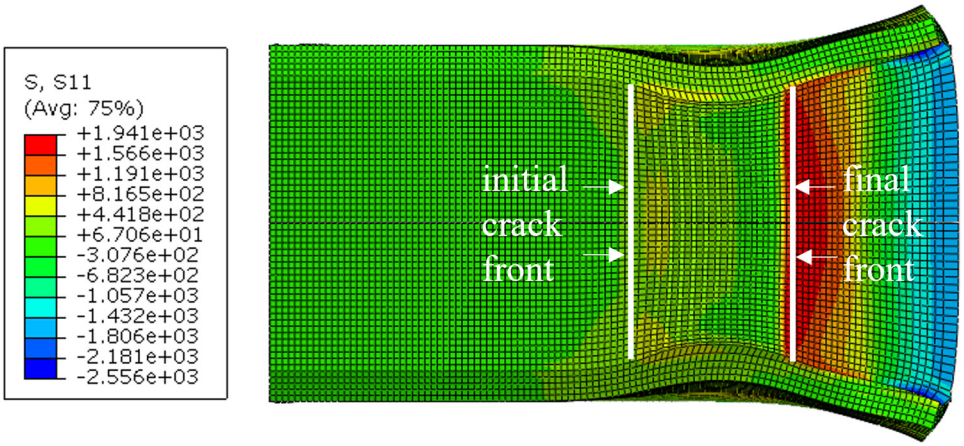

Figure 22. The fracture surface at the end of the 3-D FE simulation for the LS-2 specimen.

6. Conclusions

2-D FE Analyses with Nodal Release Method

The simulation results of the 2-D FE analyses with the nodal release method indicate that the near-tip maximum opening stress and separation work rate increase and then slightly decrease for all bend specimens. The hydrogen-charged bend specimens have lower near-tip maximum opening stresses and average separation work rates than those of the uncharged bend specimens. When the orientations of the bend specimens are considered, the uncharged LS specimen has slightly higher near-tip maximum opening stresses than those of the uncharged TS

specimen. The hydrogen-charged LS specimen has slightly lower near-tip maximum opening stresses than those of the hydrogen-charged TS specimen. In addition, the uncharged LS specimen has lower separation work rates than those of the uncharged TS specimen. The hydrogen-charged LS specimen has slightly higher separation work rates than those of the hydrogen-charged TS specimen.

2-D FE Analyses with CZM Approach

The changing near-tip maximum opening stresses and separation work rates with increasing crack extension are determined as references for the changing cohesive strengths and energies, respectively. The stress triaxiality dependency and the 3-D thickness effects enter into the TSL through the changing cohesive strength and cohesive energy based on the trends of the near-tip maximum opening stress and separation work rate obtained from the nodal release method.

The simulation results of the 2-D FE analyses with the calibrated changing cohesive parameters can match well with the test results. The hydrogen-charged specimens have the lower changing T_0 curves compared with those of the uncharged specimens. The hydrogen-charged specimens have either lower or similar changing Γ_0 curves compared with those of the uncharged specimens. When the orientations of the specimens are considered, the uncharged and hydrogen-charged LS specimens have lower cohesive strengths T_0's and $\overline{T}_0$'s than those of the uncharged and hydrogen-charged TS specimens, respectively. The uncharged LS specimen has higher cohesive energies Γ_0 and $\overline{\Gamma}_0$ than those of the uncharged TS specimen. The hydrogen-charged LS specimen has lower cohesive energies Γ_0 and $\overline{\Gamma}_0$ than those of the hydrogen-charged TS specimen.

3-D FE Analysis with Nodal Release Method

The distributions of the out-of-plane stresses and stress triaxialities in front of the growing crack fronts from the 3-D FE analysis with the nodal release method suggest that the loss of the plane strain conditions in the thickness direction with development of necking with increasing crack extension may be the reason for the increase of Γ_0 with increasing crack extension. The final decrease portions of Γ_0's may be related to the large drops of the specimen loads and the increases of the out-of-plane stresses near the side groove fronts or the increases of stress triaxialities with increasing crack extension under the fully yielded conditions.

The increases and decreases of the near-tip maximum opening stresses along Paths 1 to 4 in the 3-D FE analysis with the nodal release method are similar to those of the 2-D FE analysis with the nodal release method. The trend of the separation work rates from the 3-D FE analysis of the uniform crack extension with the nodal release method is similar to that of the 2-D FE analysis with the nodal release method. The maximum values of the stress triaxiality α along Path 1 (center plane) in the 3-D FE analysis are smaller than those in the 2-D FE analysis with the nodal release method. Also, the simulation results show a decrease part of the maximum values of α for crack extension less than 1 mm along Path 1 (center plane) in the 3-D FE analysis, which cannot be observed from the 2-D FE analysis with the nodal release method.

Acknowledgement

This work was produced by Battelle Savannah River Alliance, LLC under Contract No. 89303321CEM000080 with the U.S. Department of Energy. Publisher acknowledges the U.S. Government license to provide public access under the DOE Public Access Plan

(http://energy.gov/downloads/doe-public-access-plan). We appreciate helpful discussions with Dr. S.-J. Sung for this work.

Compliance with Ethical Standards

The authors declare that they have no conflict of interest.

References

Andersen RG, Felter CL, Nielsen KL (2019) Micro-mechanics based cohesive zone modeling of full scale ductile plate tearing: From initiation to steady-state. Int J Solids Struct 160:265–75. https://doi.org/10.1016/j.ijsolstr.2018.10.027

Anvari M, Scheider I, Thaulow C (2006) Simulation of dynamic ductile crack growth using strain-rate and triaxiality-dependent cohesive elements. Eng Fract Mech 73(15):2210-28. https://doi.org/10.1016/j.engfracmech.2006.03.016

ASTM Standard E647-15e1 (2015) Standard test method for measurement of fatigue crack growth rates. https://doi.org/10.1520/E0647-15E01.2

ASTM Standard E1820-20 (2020) Standard test method for measurement of fracture toughness. https://doi.org/10.1520/E1820-20

Banerjee A, Manivasagam R (2009) Triaxiality dependent cohesive zone model. Eng Fract Mech 76(12):1761-70. https://doi.org/10.1016/j.engfracmech.2009.03.009

Cornec A, Scheider I, Schwalbe KH (2003) On the practical application of the cohesive model. Eng Fract Mech 70:1963–87. https://doi.org/10.1016/S0013-7944(03)00134-6

Gurson AL (1977) Continuum theory of ductile rupture by void nucleation and growth: Part I—Yield criteria and flow rules for porous ductile media. ASME J Eng Mater Technol 99(1):2-15. https://doi.org/10.1115/1.3443401

Kim Y, Chao YJ, Pechersky MJ, Morgan M (2004) C-specimen fracture toughness testing: effect of side grooves and η factor. ASME J Press Vessel Technol 126(3):293–9. https://doi.org/10.1115/1.1762425

Needleman A and Tvergaard V (1987) An analysis of ductile rupture modes at a crack tip. J Mech Phys Solids 35(2):151-83. https://doi.org/10.1016/0022-5096(87)90034-2

Park K, Paulino GH, Roesler JR (2009) A unified potential-based cohesive model of mixed-mode fracture. J Mech Phys Solids 57:891–908. https://doi.org/10.1016/j.jmps.2008.10.003

Park K, Paulino GH (2012) Computational implementation of the PPR potential-based cohesive model in ABAQUS: Educational perspective. Eng Fract Mech 93:239–62. https://doi.org/10.1016/j.engfracmech.2012.02.007

Rashid FM, Banerjee A (2017) Simulation of fracture in a low ductility aluminum alloy using a triaxiality dependent cohesive model. Eng Fract Mech 179:1-12. https://doi.org/10.1016/j.engfracmech.2017.04.028

Rice JR (1968) A path independent integral and the approximate analysis of strain concentration by notches and cracks. ASME J Appl Mech 35:379–88. https://doi.org/10.1115/1.3601206

Roychowdhury S, Arun Roy YD, Dodds RH (2002) Ductile tearing in thin aluminum panels: experiments and analyses using large-displacement, 3-D surface cohesive elements. Eng Fract Mech 69:983–1002. https://doi.org/10.1016/S0013-7944(01)00113-8

Scheider I, Brocks W (2003) Simulation of cup-cone fracture using the cohesive model. Eng Fract Mech 70:1943–61. https://doi.org/10.1016/S0013-7944(03)00133-4

Scheider I, Brocks W (2006) Cohesive elements for thin-walled structures. Comput Mater Sci 37:101–9. https://doi.org/10.1016/j.commatsci.2005.12.042

Schwalbe KH, Scheider I, Cornec A (2013) Guidelines for applying cohesive models to the damage behaviour of engineering materials and structures. Springer Berlin Heidelberg.

Siegmund T, Brocks W (1999) Prediction of the work of separation and implications to modeling. Int J Fract 99(1):97-116. https://doi.org/10.1023/A:1018300226682

Siegmund T, Brocks W (2000a) The role of cohesive strength and separation energy for modeling of ductile fracture. ASTM Spec Tech Publ 139–51. https://doi.org/10.1520/STP13400S

Siegmund T, Brocks W (2000b) A numerical study on the correlation between the work of separation and the dissipation rate in ductile fracture. Eng Fract Mech 67(2):139-54. https://doi.org/10.1016/S0013-7944(00)00054-0

Sung S-J, Pan J, Korinko PS, Morgan M, McWillliams (2019) Simulations of fracture tests of uncharged and hydrogen-charged additively manufactured 304 stainless steel specimens using cohesive zone modeling. Eng Fract Mech 209:125–46. https://doi.org/10.1016/j.engfracmech.2019.01.006

Sung S-J, Wu S, Pan J, Korinko PS (2021a) Simulations of crack extensions in small arc-shaped tension specimens of uncharged and hydrogen-charged 21-6-9 austenitic stainless steels using nodal release method. ASME Press Vessel Pip Div PVP 2021-62648. https://doi.org/10.1115/PVP2021-62648

Sung S-J, Wu S, Pan J (2021b) Separation work rate for crack extension in a thin compact tension specimen with finite step nodal release method. ASME Press Vessel Pip Div PVP 2021-62656. https://doi.org/10.1115/PVP2021-62656

Woelke PB, Shields MD, Hutchinson JW (2015) Cohesive zone modeling and calibration for mode I tearing of large ductile plates. Eng Fract Mech 147:293–305. https://doi.org/10.1016/j.engfracmech.2015.03.015

Wu S, Pan J, Korinko PS, Morgan M (2020) Simulations of crack extensions in arc-shaped tension specimens of uncharged and tritium-charged-and-decayed 21-6-9 austenitic stainless steels using cohesive zone modeling. ASME Press Vessel Pip Div PVP 2020-43542. https://doi.org/10.1115/PVP2020-21737

Wu S, Pan J, Korinko PS, Morgan M (2021) Simulations of crack extensions in arc-shaped tension specimens of uncharged and hydrogen-charged 21-6-9 austenitic stainless steels using cohesive zone modeling with varying cohesive parameters. Eng Fract Mech 245:107603. https://doi.org/10.1016/j.engfracmech.2021.107603

Zhang T, Yuan H, Yang S (2020) Fracture energy and tensile strength depending on stress triaxiality along a running crack front in three-dimensional cohesive modeling. Eng Fract Mech 227:106919. https://doi.org/10.1016/j.engfracmech.2020.106919

Appendix A: 2-D FE Analyses to Simulate Crack Extensions by Nodal Release

Figure A1 shows the FE model of the right half of the LS-2 specimen. The FE model shown in Figure A1 is the same as the one shown in Figure 6 except only the right half of the specimen without cohesive elements is modeled due to the symmetry conditions. Figure A1 shows the symmetry condition, marked in blue, applied to the ligament. The FE models for the other three bend specimens are similar and will not be shown here. The crack tip opening displacement (CTOD) is in the order of $J_{0.2}/\sigma_0$. The size of the elements of 0.1 mm by 0.1 mm near the crack plane is in the order of the CTOD in order to determine the near-tip maximum opening stress at about one element away from the growing crack tip with the geometry nonlinearity.

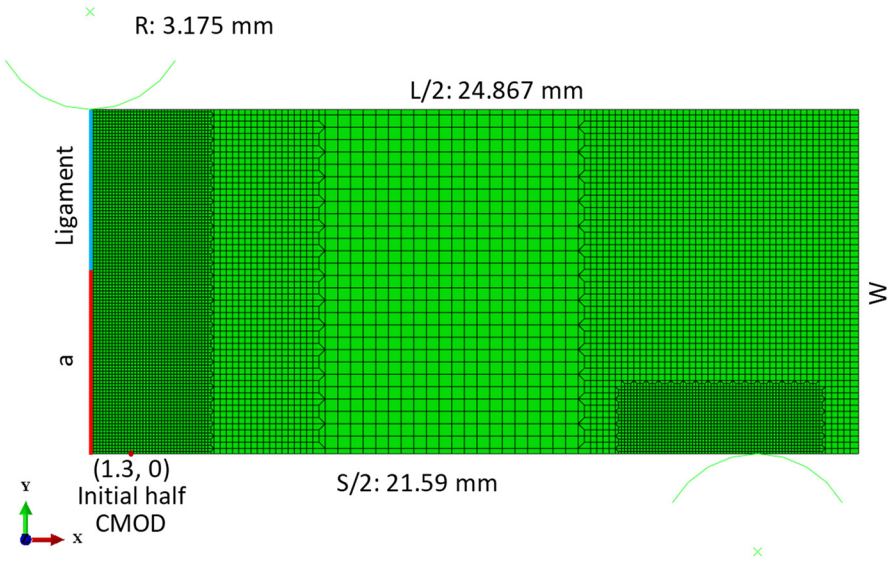

Figure A1. The FE model of the right half of the LS-2 specimen.

The boundary conditions of the FE analyses are controlled by the multiple-linear Δa vs pin displacement curves. The crack extension is controlled by decreasing the length of the symmetry condition. The available experimental displacement data are the CMODs. The pin displacement boundary is applied to the center of the loading pin. Several rounds of the

iterations are necessary to obtain the crack extension vs pin displacement curves to give the multiple-linear Δa vs CMOD curves measured during the experiments. Figures A2(a) and A2(b) show the computational multiple-linear Δa vs CMOD curves for the LS-2 and LS-4 specimens, respectively. The computational multiple-linear Δa vs CMOD curve for the 3-D FE analysis for the LS-2 specimen as presented in Section 5 is also shown in Figure A2(a). It should be mentioned that the CMODs from the 3-D FE analysis are relatively uniform through the thickness of the specimen along the *Z* direction. Therefore, the CMODs are taken from the specimen surface from the 3-D FE analysis. Figures A3(a) and A3(b) show the computational multiple-linear Δa vs CMOD curves for the TS-2 and TS-4 specimens, respectively. Figures A2 and A3 show that the entire simulation is divided into several steps. During each step, the loading pin is moving downward and a finite length of the symmetry condition (the remaining ligament) is also released to propagate the crack to give the computational Δa vs CMOD curve for comparison with the test results.

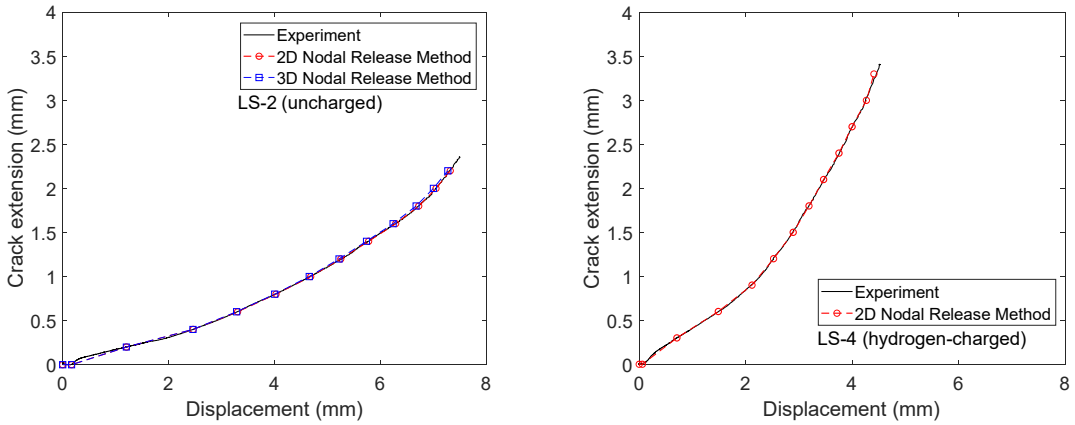

Figure A2. The experimental and computational Δa vs CMOD curves for the (a) LS-2 specimen and (b) LS-4 specimen.

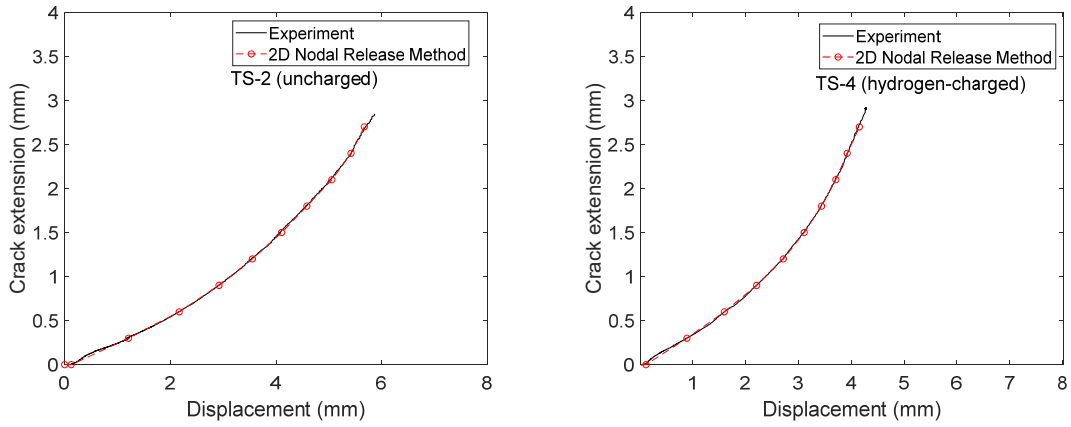

(a) (b)

Figure A3. The experimental and computational Δa vs CMOD curves for the (a) TS-2 specimen and (b) TS-4 specimen.

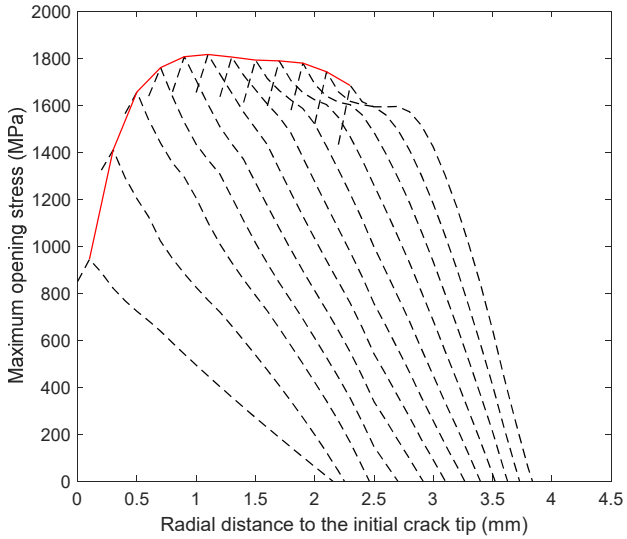

Figure A4. The opening stresses and near-tip maximum opening stresses for the LS-2 specimen.

The changing cohesive strengths can be referenced by examining the changing near-tip maximum opening stresses. The opening stresses σ_{xx}'s in front of the crack tips at the ends of crack extension steps for the LS-2 specimen is shown in Figure A4. Here, the black dotted lines represent the opening stresses in front of the crack tips and the red solid line represents the connections of the near-tip maximum opening stress locations in front of the growing crack tip. The σ_{xx} distributions for the LS-4, TS-2 and TS-4 bend specimens are similar and will not be

shown here. However, for convenience of comparison, Figure A5(a) shows the near-tip maximum opening stresses and their locations at the ends of the crack extension steps for the LS-2 and LS-4 specimens. Here, the near-tip maximum opening stresses increase from the small values below 1,000 MPa near crack initiation to the large values about 1,815 MPa and 1,587 MPa at about 1 mm in front of the initial crack tips and then decrease with increasing crack extension for the LS-2 and LS-4 specimens, respectively. The near-tip maximum opening stresses for the LS-2 specimen in Figure A5(a) from the 2-D FE analysis are similar to those from the 3-D FE analysis shown in Figure 19. For comparison, the near-tip maximum opening stresses along Path 1 (center plane) for the LS-2 specimen from the 3-D FE analysis are shown in Figure A5(a). As shown in Figure A5(a), the near-tip maximum opening stresses of the LS-4 specimen is lower than those of the LS-2 specimen.

The changing cohesive energies can be referenced by examining the changing separation work rates in the 2-D plane strain FE analyses of the half specimens as explained in the following. Here, the balance of the energies of the system can be written as

$$W_{\text{ext}} = U_e + W_p + W_s \tag{A1}$$

where W_{ext} is the external work, U_e is the elastic strain energy, W_p is the plastic dissipation, and W_s is the separation work for creating a new free surface. For each step, Equation (A1) can be written as

$$\Delta W_{\text{ext}} = \Delta U_e + \Delta W_p + \Delta W_s \tag{A2}$$

where ΔW_{ext} is the change of external work, ΔU_e is the change of elastic strain energy, ΔW_p is the change of plastic dissipation, and ΔW_s is the change of separation work for creating a new free surface. For each step with a crack area increment ΔA, Equation (A2) can be written as

$$\frac{\Delta W_{\text{ext}}}{\Delta A} = \frac{\Delta U_e}{\Delta A} + \frac{\Delta W_p}{\Delta A} + \frac{\Delta W_s}{\Delta A} \tag{A3}$$

Here, $\frac{\Delta W_{\text{ext}}}{\Delta A}$ represents the average external work rate for a crack area increment, $\frac{\Delta U_e}{\Delta A}$ represents the average elastic strain energy rate for a crack area increment, $\frac{\Delta W_p}{\Delta A}$ represents the average plastic dissipation rate for a crack area increment, and $\frac{\Delta W_s}{\Delta A}$ represents the average separation work rate for a crack area increment.

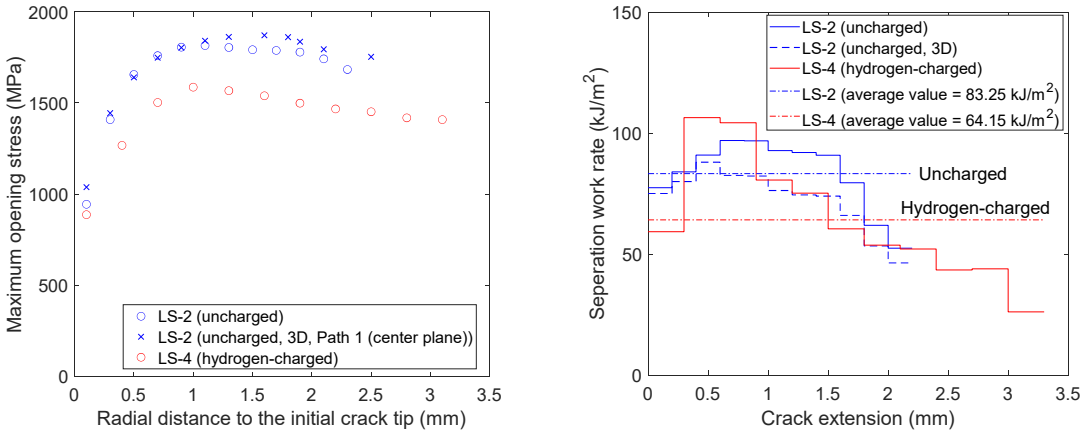

Figure A5. (a) The near-tip maximum opening stresses and their locations and (b) the separation work rates for the LS-2 specimen and LS-4 specimen.

It should be mentioned that in ABAQUS, the change of separation work, ΔW_s, can be calculated by using the nodal forces and nodal displacements at the released nodes for each step. The calculated separation work rate can also be validated by Equation (A3) from the values of $\frac{\Delta W_{\text{ext}}}{\Delta A}$, $\frac{\Delta U_e}{\Delta A}$, and $\frac{\Delta W_p}{\Delta A}$ for the known change of crack area in each step. The separation work rates per unit increase of crack area are plotted for the crack extension steps for the LS-2 and LS-4 specimens in Figure A5(b). As shown in Figure A5(b), the separation work rates increase from

small values to reach the maximum values near the crack extensions of about 1.0 mm and 0.6 mm for the LS-2 and LS-4 specimens, respectively. The separation work rates then decrease with increasing crack extension. In Figure A5(b), the separation work rates for the LS-2 specimen from the 3-D FE analysis of the uniform crack extension by nodal release are also shown. The 3-D FE analysis is discussed in Section 5. As shown in Figure A5(b), the trends of the separation work rates from both 2-D and 3-D FE analyses are very similar.

The average separation work rate $\overline{\dot{W}_s}$ is defined as

$$\overline{\dot{W}_s} = \frac{\sum \Delta W_s}{(\Delta a)_f \, B_n} \tag{A4}$$

where $\sum \Delta W_s$ represents the summation of the separation works for all steps, $(\Delta a)_f$ represents the final crack growth of the simulation, and B_n represents the net thickness of the specimen. The values of the average separation work rates of the LS-2 and LS-4 specimens are also plotted in Figure A5(b). The average separation work rate of the LS-4 specimen is lower than that of the LS-2 specimen.

Similarly, Figures A6(a) and A6(b) show the near-tip maximum opening stresses and separation work rates for the TS-2 and TS-4 specimens, respectively. Figure A6(a) shows that the near-tip maximum opening stresses increase from the small values about 1,000 MPa near cack initiation to the large values about 1,764 MPa and 1,624 MPa near the crack extension of about 1.3 mm in front of the initial crack tips and then decrease with increasing crack extension for the TS-2 and TS-4 specimens, respectively. Similarly, the near-tip maximum opening stresses of the TS-4 specimen is lower than those of the TS-2 specimen. Figure A6(b) shows that the separation work rates increase from small values to reach the maximum values near the crack extensions of about 0.6 mm and 0.8 mm for the TS-2 and TS-4 specimens, respectively. The

separation work rates then decrease with increasing crack extension. Similarly, the values of the average separation work rates of the TS-2 and TS-4 specimens are also plotted in Figure A6(b). The average separation work rate of the TS-4 specimen is lower than that of the TS-2 specimen.

It should be mentioned that in the CZM approach, the changing cohesive strengths of the cohesive elements should be lower than or close to the near-tip maximum opening stresses. Otherwise, the cohesive elements ahead of the growing crack tips will not open up as suggested in Sung et al. (2021a). Since the separation of the cohesive elements ahead of the growing crack tips results in less plastic dissipation in the neighboring continuum elements, the separation work rate obtained from the 2-D FE analysis is not the same as the cohesive energy. However, the trend of increasing and decreasing separation work rate with increasing crack extension can still be used as reference for the calibration of the changing cohesive energy.

The lower near-tip maximum opening stresses and average separation work rates of the hydrogen-charged specimens when compared with those of the uncharged specimens indicate the effect of hydrogen on the AM steels. Also, a comparison of the near-tip maximum opening stresses in Figures A5(a) and A6(a) indicate that the uncharged LS specimen has higher near-tip maximum opening stresses than those of the uncharged TS specimen. The hydrogen-charged LS specimen has slightly lower near-tip maximum opening stresses than those of the hydrogen-charged TS specimen. Also, Figures A5(b) and A6(b) indicate that the uncharged LS specimen has lower separation work rates than those of the uncharged TS specimen. The hydrogen-charged LS specimen has slightly higher separation work rates than those of the hydrogen-charged TS specimen.

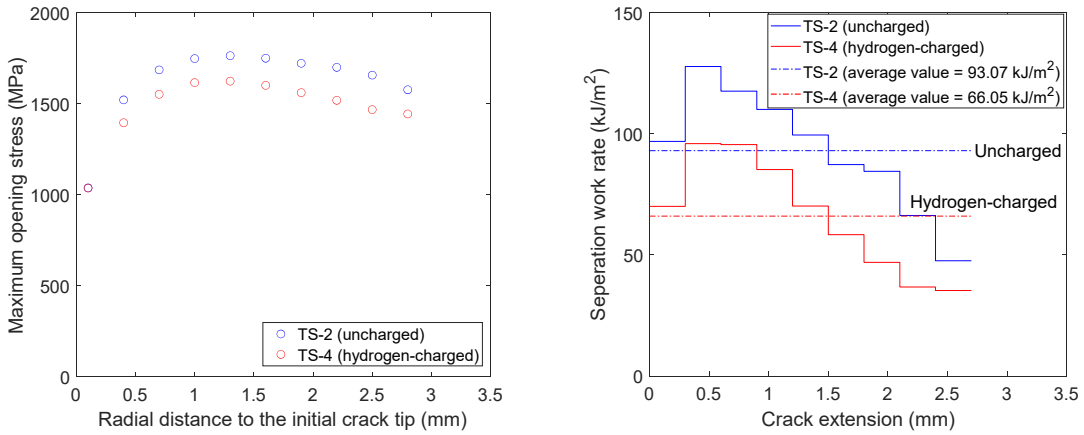

Figure A6. (a) The near-tip maximum opening stresses and their locations and (b) the separation work rates for the TS-2 specimen and TS-4 specimen.

Figures A7 and A8 show the stress triaxialities α's and the maximum stress triaxialities in front of the growing crack tips for the LS and TS bend specimens, respectively. Here, the black dotted lines represent the α distribution in front of the growing crack tips and the red solid lines represent the connections of the maximum stress triaxiality locations in front of the growing crack tips. The simulation results indicate that the maximum values of α increase and then decrease with increasing crack extension. The maximum values of α in front of the growing crack tips increase from 2.11 to 4.15, 2.10 to 3.39, 2.08 to 3.51, and 2.09 to 3.15 for the LS-2, LS-4, TS-2, and TS-4 specimens, respectively. For a reference, the stress triaxiality for the asymptotic crack tip stresses for an elastic perfectly plastic material under plane strain conditions can be calculated as 2.39 (Rice 1968).

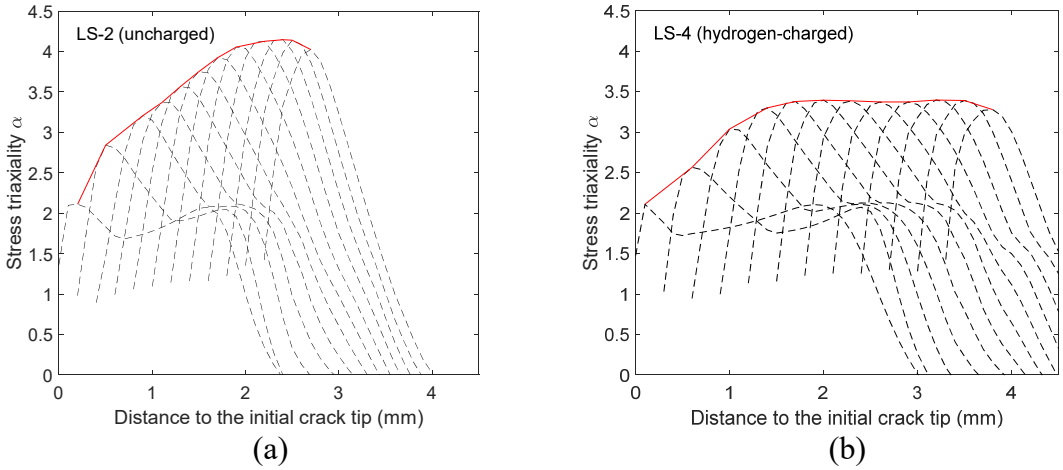

Figure A7. The stress triaxiality in front of the growing crack tips for the (a) LS-2 specimen and (b) LS-4 specimen.

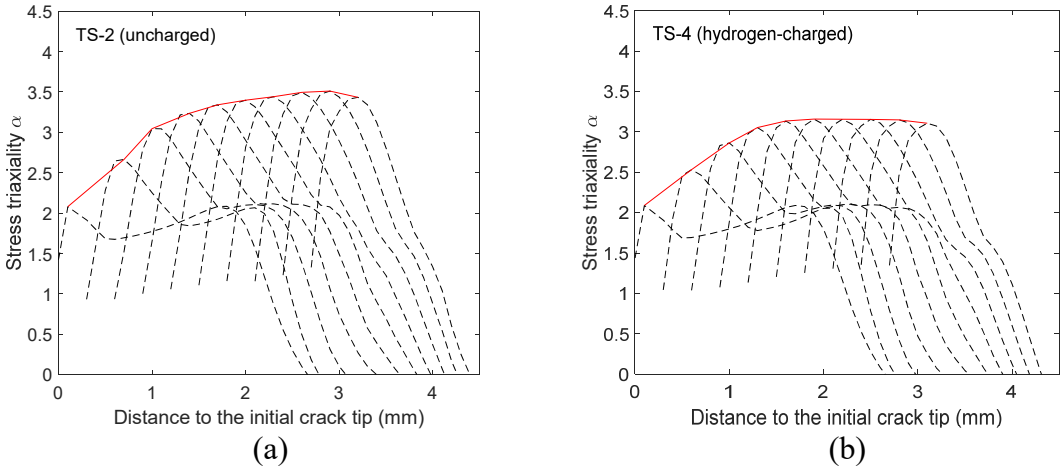

Figure A8. The stress triaxiality in front of the growing crack tips for the (a) TS-2 specimen and (b) TS-4 specimen.

The stress triaxiality can be a factor to determine the magnitude of cohesive energy as suggested by Siegmund and Brocks (2000a). In general, the cohesive energy is lower when the stress triaxiality is higher according to the Gurson material model for ductile fracture as discussed in Siegmund and Brocks (2000a). However, from the energy balance viewpoint based on the test results, the separation work rate increases and then decreases with increasing crack extension. Therefore, the stress triaxiality may not be the dominant factor to contribute to the

changing separation work rate or the changing cohesive energy according to the 2-D FE analyses. The loss of plane strain conditions in the thickness direction with development of necking with increasing crack extension may be the more dominant factor for the initial increasing separation work rate or the initial increasing cohesive energy based on the results of the 3-D FE analysis of the uniform crack extension by nodal release as discussed in Section 5. The final decreasing separation work rates or cohesive energies may be related to the large drops of the specimen loads and increasing out-of-plane stresses near the side grooves or the increasing stress triaxialities under fully yield conditions as discussed in Section 5.

In summary, the near-tip maximum opening stress and separation work rate from the 2-D FE analyses by nodal release show the loading capacity of the material elements ahead of the growing crack tip and the required energy balance of the entire specimen for the stress-state dependent crack growth. The effects of the thickness, side grooves and necking give the changing near-tip maximum opening stress and separation work rate from the 2-D FE analyses by nodal release. Therefore, the effects of stress triaxiality and the thickness enter into the TSL through the changing cohesive strength and cohesive energy based on the trends of the near-tip maximum opening stress and separation work rate from the 2-D FE analyses with nodal release.